ADVANCED MATERIALS

Supporting Information

for *Adv. Mater.,* DOI: 10.1002/adma.202212069

2D Nano-Sonosensitizers Facilitate Energy Transfer to Enhance Sonodynamic Therapy

*Gan Lin, Geoffrey T. Nash, Taokun Luo, Indranil Ghosh, Siddhartha Sohoni, Andrew J. Christofferson, Gang Liu, Gregory S. Engel, and Wenbin Lin**

Supporting Information for

Two-Dimensional Nanosonosensitizers Facilitate Energy Transfer to Enhance Sonodynamic Therapy

Gan Lin,[‡] Geoffrey T. Nash,[‡] Taokun Luo,[‡] Indranil Ghosh, Siddhartha Sohoni, Andrew J. Christofferson, Gang Liu, Gregory S. Engel, Wenbin Lin,[*]

*Gan Lin, Geoffrey T. Nash, Taokun Luo, Indranil Ghosh, Siddhartha Sohoni, Andrew J. Christofferson, Gang Liu, Gregory S. Engel, Wenbin Lin**

Dr. G. Lin, G. T. Nash, T. Luo, I. Ghosh, S. Sohoni, Prof. G. S. Engel, Prof. W. Lin
Department of Chemistry, The University of Chicago, Chicago, IL 60637, USA
E-mail: wenbinlin@uchicago.edu

Dr. G. Lin, Prof. G. Liu
State Key Laboratory of Molecular Vaccinology and Molecular Diagnostics & Center for Molecular Imaging and Translational Medicine, School of Public Health, Xiamen University, Xiamen 361102, China

Dr. A. J. Christofferson
School of Science, College of Science, Engineering and Health, RMIT University, Melbourne, Victoria 3001, Australia

Prof. G. S Engel
Pritzker School of Molecular Engineering, The University of Chicago, Chicago, IL 60637, USA

Prof. W. Lin
Department of Radiation and Cellular Oncology and Ludwig Center for Metastasis Research, The University of Chicago, Chicago, IL 60637, USA

[‡]Equal contribution

*Corresponding author; Email: wenbinlin@uchicago.edu

S1. Experiment section

1.1. Chemicals and methods

All starting materials were purchased from Sigma-Aldrich and Thermo Fisher Scientific (USA) and used without further purification unless otherwise specified. Transmission electron microscopy (TEM) was performed on a TECNAI Spirit TEM. Atomic force microscopy (AFM) was performed on a Bruker Multimode 8-HR instrument. Powder X-ray diffraction (PXRD) patterns were obtained on a Bruker D8 Venture diffractometer using a Cu Kα radiation source (λ = 1.54178 Å) and processed with PowderX software. Dynamic light scattering (DLS) and zeta potential measurements were obtained on a Malvern Zetasizer Nano ZS instrument. Inductively coupled plasma-mass spectrometry (ICP-MS) was performed on an Agilent 7700x ICP-MS and analyzed using ICP-MS Mass Hunter version 4.6 C.01.06. Samples were diluted in a 2% HNO_3 matrix and analyzed with ^{159}Tb and internal standards against a 10-point standard curve between 1 ppb and 500 ppb. The correlation coefficient was R>0.999 for all analyses of interest. Data collection was performed in spectrum mode with three replicates per sample and 100 sweeps per replicate. ^{1}H and ^{19}F NMR spectra were collected on a Bruker NMR 400 DRX spectrometer at 400 MHz and referenced to the proton resonance resulting from incomplete deuteration of $CDCl_3$ (δ 7.26) or DMSO-d_6 (δ 2.50). Matrix-assisted laser desorption/ionization-time of flight high resolution mass spectrometry (MALDI-TOF HRMS) was performed on a Bruker autoflex maX MALDI-TOF/TOF using positive-ion reflectron mode.

UV-Vis spectroscopy data was collected on a Shimadzu UV-2600 spectrophotometer. Steady-state fluorescence emission spectra were obtained on a HORIBA Fluorolog-3 spectrofluorometer equipped with a Synapse OE-CCD detector. Spectral overlap integrals were calculated using a|e – UV-Vis-IR Spectral Software 1.2 (FluorTools, DK).

US irradiation was given using a Chattanooga Intelect TranSport Ultrasound (Model 2782). The fluorescence intensity of SOSG was measured using a Synergy HTX plate reader (Agilent Technologies, USA). DPBS-$Mg^{2+}$and -Ca^{2+} were purchased from Thermo Fisher Scientific. Trypsin-EDTA solution was purchased from ATCC. 3-(4,5- dimethylthiazol-2-yl)-5-(3-carboxy-methoxyphenyl)-2-(4-sulfo-phenyl)2H-tetrazolium (MTS) assay was purchased from Promega (USA). Murine colorectal carcinoma CT26 cells and murine triple negative breast cancer cell line 4T1 were purchased from the American Type Culture Collection (ATCC, Rockville, MD). CT26 and 4T1 cells were cultured in RPMI-1640 (Corning, USA) and supplemented with 10% filtered fetal bovine serum (VWR, USA) and 1% HyClone Penicillin-Streptomycin 100X solution (Cytiva, USA). The cells were kept in a water-jacketed incubator with 100% humidity and 5% CO_2 at 37°C. Flow cytometry data was collected on an LSR-Fortessa 4-15 (BD Biosciences, USA) and analyzed with FlowJo software (Tree Star, USA). Confocal laser scanning microscope images were collected on a Leica Stellaris 8 laser scanning confocal microscope. CLSM imaging was performed at the University of Chicago Integrated Light Microscopy Facility and analysis was done with ImageJ software (NIH, USA). The histological slides were scanned on a CRi Pannoramic SCAN 40x whole slide scanner by Integrated Light Microscopy Core in the University of Chicago and analyzed with the QuPath-0.2.3 software.[1] The absorbance and fluorescence from well plates were read by a BioTek Synergy HTX microplate reader. BALB/c breeders were obtained from Charles River Laboratories (USA) and bred in house at the animal facility at the University of Chicago. BALB/c mice with an age of 6-8 weeks were used for *in vivo* experiments. The study protocol was reviewed and approved by the Institutional Animal Care and Use Committee (IACUC) at the University of Chicago. The Human Tissue Resource Center at the University of Chicago provided the histology related services for this study.

1.2. Synthesis and characterization of Hf_{12}-DBB-Ir (MOL)

Synthesis of DBB-Ir. $Ir(DBB)[dF)CF_3)ppy]_2^+$ [DBB-Ir, DBB = 4,4'-di(4-benzoato)-2,2'- bipyridine; $dF(CF_3)ppy$ = 2-(2,4-difluorophenyl)-5-(trifluoromethyl)pyridine] was synthesized as shown in Figure S1 according to a previous literature report.[2] ^{1}H NMR (400 MHz, DMSO-d_6): δ 9.10 (d, 2H), 8.77 (dd, 2H), 8.49 (d, 2H), 8.44 (d, 2H), 8.16 (s, 2H), 8.04 (d, 4H), 7.82 (s, 2H), 7.65 (d, 4H), 7.11 (m, 2H), 5.91 (dd, 2H).

Synthesis of Hf_{12}-DBB-Ir (MOL). The MOL was synthesized according to a previous literature report with minor modifications.[3] To a 1-dram glass vial was added 0.5 mL of $HfCl_4$ solution [2.0 mg/mL in *N,N*-dimethylformamide (DMF)], 0.5 mL of DBB-Ir solution (4.0 mg/mL in DMF), 2 μL of trifluoroacetic acid (TFA), and 7 μL of water. The mixture was briefly sonicated and then kept in an 80 °C oven for 1 day. The yellow solid was collected by centrifugation and washed sequentially with DMF and ethanol and then stored as an ethanol dispersion in the dark.

NMR analysis of the digested MOL. 1.0 mg of MOL was dried under vacuum. A solution of 500 μL DMSO-d_6 and 50 μL D_3PO_4 was added to the dried solid. The mixture was then sonicated for about 10 min, until no solid residue remained. Prior to ^{1}H NMR analysis, 50 μL D_2O was added to the mixture.

1.3. Synthesis and characterization of TBP@MOL

Synthesis of TBP@MOL. To a 1-dram glass vial was added 1.0 mL of MOL solution (4.29 mM in ethanol based on Hf), 1.0 mL of 5,10,15,20-tetra(*p*-benzoato)porphyrin (TBP) solution (0.8 mg/mL in DMF), and a stir bar. The mixture was stirred at room temperature overnight. The resulting red solid was collected by centrifugation and washed sequentially with DMF and ethanol and then stored as an ethanol dispersion in the dark.

UV-Vis analysis of TBP@MOL. 10 μL of a dispersed solution of TBP@MOL was added to a mixture of 940 μL DMSO and 50 μL H_3PO_4. The mixture was then sonicated for about 10 minutes and the UV-Vis absorption spectrum was recorded.

ICP-MS analysis of TBP@MOL. 10 μL of a dispersed solution of TBP@MOL was added to a mixture of 980 μL HNO_3 and 10 μL HF. The mixture was vortexed, kept at room temperature for 3 days and then analyzed.

Determination of TBP loading in TBP@MOL. The weight % loading of TBP in TBP@MOL was calculated to be 12.3% using UV-Vis spectroscopy to determine the TBP concentration (378.8 μM), from the Soret band at 420 nm, and ICP-MS to determine the Hf concentration (2.69 mM). The TBP:Hf_{12} SBU ratio was about 1.7:1, which yielded the ideal formula $(TBP)_{1.7}@Hf_{12}(O)_8(OH)_8(DBB\text{-}Ir)_6(TFA)_{4.3}$. This formula was also supported by the partially reduced integration of the TFA fluorine signal at δ = -74.23 ppm in the ^{19}F NMR spectrum of TBP@MOL compared to the MOL.

1.4. Synthesis and characterization of DBP@MOL

Synthesis of DBP@MOL. To a 1-dram glass vial was added 1.0 mL of MOL solution (4.29 mM in DMF based on Hf), 1.0 mL of 5,15-di(*p*-benzoato)porphyrin (DBP) solution (1.0 mg/mL in DMF), and a stir bar. The mixture was stirred at room temperature overnight. The resulting red solid was collected

by centrifugation and washed sequentially with DMSO, DMF and ethanol and then stored as an ethanol dispersion in the dark.

Determination of DBP loading for DBP@MOL. The weight % loading of DBP in DBP@MOL was calculated to be 19.4% using UV-Vis spectroscopy to determine the DBP concentration (491.3 μM), from the Soret band at 409 nm, and ICP-MS to determine the Hf concentration (1.46 mM). The DBP:Hf_{12} SBU ratio was about 4.0:1, which yielded the ideal formula $(DBP)_{4.0}@Hf_{12}(O)_8(OH)_8(DBB\text{-}Ir)_6(TFA)_{2.0}$. This formula was also supported by the significantly reduced integration of the TFA fluorine signal at δ = -74.23 ppm in the ^{19}F NMR spectrum of DBP@MOL compared to MOL.

1.5. Synthesis and characterization of Hf-TBP and Hf-DBP MOFs

Synthesis of Hf-TBP and Hf-DBP MOFs. 5,10,15,20-tetra(*p*-benzoato)porphyrin (TBP) and 5,15-di(*p*-benzoato)porphyrin (DBP) were synthesized following previously reported methods.[4, 5] Hf-TBP and Hf-DBP MOFs were synthesized according to literature reports.[4, 6, 7]

Hf-TBP was synthesized by adding 2 mg $HfCl_4$, 1.9 mg TBP, 60 μL of 88% formic acid (FA), and 2 mL DMF to a 1-dram glass vial. The vial was placed in an 80 °C oven for 2 days. The purple suspension was collected by centrifugation, washed with DMF, 1% triethylamine in ethanol, and ethanol sequentially. The resulting Hf-TBP solid was redispersed in ethanol and stored in the dark.

Hf-DBP MOF was synthesized by adding 2 mg $HfCl_4$, 1 mg DBP, 75 μL acetic acid, and 1 mL DMF to a 1-dram glass vial. The vial was placed at 90 °C oven for 3 days. The resulting purple solid was collected by centrifugation, washed with DMF and ethanol, and stored as ethanol dispersions in the dark.

1.6. Synthesis and characterization of Hf-BTB MOL and TBP@Hf-BTB MOL

Synthesis of Hf-BTB. To a 1-dram glass vial was added 1.0 mL of $HfCl_4$ solution (2.0 mg/mL in DMF), 0.21 mL of 1,3,5-tris(4-carboxyphenyl)benzene (BTB) solution (2.0 mg/mL in DMF), 85 μL of 98% formic acid (FA), and 15 μL of water. The mixture was briefly sonicated and then kept in an 80 °C oven for 1 day. The translucent white solid was collected by centrifugation and washed sequentially with DMF and ethanol and then stored as an ethanol dispersion in the dark. The formula for Hf-BTB is $Hf_6(\mu\text{-}O)_4(\mu\text{-}OH)_4(BTB)_2(HCO_2)_6$.

Synthesis of TBP@Hf-BTB. To a 1-dram glass vial was added 0.8 mL of Hf-BTB solution (1.16 mM in ethanol based on BTB), 0.8 mL of TBP solution (0.5 mg/mL in DMF), and a stir bar. The mixture was stirred at room temperature overnight. The resulting red solid was collected by centrifugation and washed sequentially with DMF and ethanol and then stored as an ethanol dispersion in the dark.

Determination of TBP loading for TBP@Hf-BTB. The weight % loading of TBP in TBP@Hf-BTB was calculated to be 13.8% using UV-Vis spectroscopy to determine the TBP concentration (116.3 μM), from the Soret band at 420 nm, and ICP-MS to determine the Hf concentration (1.50 mM). The TBP:Hf_6 SBU ratio was about 0.47:1, which yielded the formula $(TBP)_{0.47}@Hf_6(\mu\text{-}O)_4(\mu\text{-}OH)_4(BTB)_2(HCO_2)_{5.53}$. This formula was also supported by the partially reduced integration of the FA proton signal at δ = 8.12 ppm in the ^1H NMR spectrum of TBP@Hf-BTB compared to Hf-BTB.

1.7. Photophysical Characterization

Time-domain lifetimes were measured on a ChronosBH lifetime fluorometer (ISS, Inc.) using time-correlated single photon counting (TCSPC) methods. The fluorometer contained Becker-Hickl SPC-130 detection electronics and an HPM-100-40 Hybrid PMT detector. Excitation was provided by a 403 nm picosecond pulsed laser source (Hamamatsu PLP-10) operating at a 5 MHz repetition rate. Emission wavelengths were selected with an interference filter at 550 nm with 40 nm bandpass (for DBB-Ir emission) or an interference filter at 642 nm with 10 nm bandpass (for TBP/DBP emission). The instrument response function (IRF) was measured to be approximately 120.0 ps FWHM with a 1 wt% suspension of Ludox LS colloidal silica in water. Multi-component exponential decay lifetimes were fit using the MATLAB *fit* function with the default 'Trust Region' algorithm. Goodness of fit is reported using reduced chi-squared values.

Ultrafast transient absorption spectroscopy was performed using sub-20 fs white light pump and probe pulses. A mode-locked oscillator (Coherent, Inc.) with a Ti:sapphire crystal that operates at 80 MHz seeds a Ti:sapphire regenerative amplifier (Coherent, Inc.), which in turn generates a ~40 fs pulse centered at 800 nm with a 5 kHz repetition rate. This pulse undergoes self-phase modulation in a pressurized 2 m long argon gas tube to create chirped white broadband pulses with a bandwidth ranging from 480 nm to 800 nm. Dichroic filters, bandpass filters (Thorlabs, Inc.) and chirped mirrors (Laser Quantum) are used to shape the bandwidth and temporal profile of the pulse. This results in a sub-15 fs white light pulse with a bandwidth from 500 to 730 nm. This pulse is split into pump and probe pulses, and the pump pulse is delayed temporally with respect to the probe pulse with a retroreflector on a stage up until 1 ns (Aerotech Inc.). Data is averaged over 80 runs for each sample to obtain reliable dynamics over scatter contributions due to the large sized domains of Hf-TBP and TBP@MOL in solution.

1.8. Singlet Oxygen Generation

Singlet oxygen sensor green (SOSG, Invitrogen, USA) assay was used to measure the $^1O_2$ production and sonodynamic therapy (SDT) efficacy of the sonosensitizers at various times after US irradiation. 100 μL of aqueous dispersions with equivalent doses of 2.5 μM sonosensitizer (e.g., TBP in TBP@MOL) and 15 μM SOSG solution were exposed to US irradiation (3.4 MHz, 1.0 W/cm^2, 50% duty cycle) for 0, 1, 2.5, 5, and 10 minutes, and the SOSG fluorescence intensity was measured at each time point using a fluorescence plate reader (λ_{ex} = 485, λ_{em} = 520 nm). The controls for MOL and Hf-BTB were prepared using equivalent doses of either DBB-Ir (6.32 μM) or BTB (29.4 μM) as the TBP@MOL and TBP@Hf-BTB groups, respectively. The mixture of TBP and MOL control group was prepared using equivalent TBP (2.5 μM) and DBB-Ir (6.32 μM) doses as in TBP@MOL.

SOSG assay was also used to measure the $^1O_2$ production and photodynamic therapy (PDT) efficacy of the sensitizers at various times after visible light irradiation. Aqueous dispersions (1 mL total volume) of the sensitizers, with equivalent doses of 1.5 μM for TBP or 2.5 μM for DBP, in the presence of 15 μM SOSG were prepared. 100 μL aliquots (n = 5) of the resulting dispersions were added to a 96-well plate and were exposed to visible light irradiation (630 nm, 100 mW/cm^2) for 0, 1, 2, 3, 5, 7, 10, and 15 minutes, and the SOSG fluorescence intensity was measured at each time point using a fluorescence plate reader (λ_{ex} = 485, λ_{em} = 520 nm).

1.9. Reactive Oxygen Species and Hydroxyl Radicals Generation

Dichlorofluorescein (DCF, Invitrogen, USA) and 3′-(p-hydroxyphenyl) fluorescein (HPF, Invitrogen, USA) assays were used to detect total reactive oxygen species (ROS) and hydroxyl (•OH) radicals in

different TBP systems after US irradiation. 100 μL of aqueous dispersions with equivalent doses of 2.5 μM sonosensitizer (e.g., TBP in TBP@MOL) and 10 μM DCF (or HPF) solution were exposed to US irradiation (3.4 MHz, 1.0 W/cm^2, 50% duty cycle) for 0, 1, 2.5, 5, and 10 minutes, and the DCF (or HPF) fluorescence intensity was measured at each time point using a fluorescence plate reader (λ_{ex} = 485, λ_{em} = 520 nm).

1.10. In Vitro Study

Cell viability assay

The US irradiated [denoted as (+)] and US free [denoted as (-)] cytotoxicities of TBP, Hf-TBP, TBP@MOL, and MOL were assessed on CT26 and 4T1 cells using 3-(4,5- dimethylthiazol-2-yl)-5-(3-carboxymethoxyphenyl)-2-(4-sulfo-phenyl)-2H-tetrazolium (MTS) assay (Promega, USA). Cells were seeded on 96-well plates at a density of 2000 cells/well and further cultured overnight. TBP, Hf-TBP or TBP@MOL was added to the wells at equivalent TBP concentrations of 0, 2.5, 5.0, 7.5, 10, 20, 40, 60, 80 μM and incubated for 6 hours (n = 4), followed by US irradiation (3.4 MHz, 1 W/cm^2, 50% duty cycle) for 10 minutes. MOL was added to the wells at an equivalent DBB-Ir concentration of 0, 8.75, 17.5, 26.3, 35, 70, 140, 210, 280 μM, followed by the same US treatment as above. Cells were further incubated for 24 hours and subject to cell viability measurement using MTS assay. The IC_{50} value was determined by fitting the dose response curves in Origin Lab.

Cellular uptake

Cellular uptakes of TBP, Hf-TBP and TBP@MOL were evaluated on CT26 cells. Cells were seeded on 6-well plates at a density of 5×10^5 and cultured in DMEM medium (10%) overnight. TBP, Hf-TBP or TBP@MOL was added to each well with final equivalent TBP concentrations of 10 μM (n = 3). Cells were cultured in the 37 ℃ incubator. At different time points (1, 2, 4, 8 h), the medium was removed and the cells were washed three times with PBS, trypsinized and collected by centrifugation. After counting by a hemocytometer, cells were digested with 1 mL of DMSO (containing 10% H_3PO_4) in 1.5 mL Eppendorf tubes for 48 hours, with strong sonication every 12 hours. The TBP concentration was determined by UV-Vis absorbance at 420 nm according to the established standard curve.

In vitro ROS generation

The ROS generation from SDT treatment was evaluated on CT26 cells by flow cytometry and CLSM. For flow cytometry experiments, CT26 cells were seeded at a density of 5×10^5 cells/mL in 6-well plates and the cells were treated with TBP, Hf-TBP and TBP@MOL at equivalent TBP concentrations of 5 μM and further incubated for 6 hours. 20 μM DCF-DA (Invitrogen) was then added to each well for another 1 hour incubation. The plates were then treated with US irradiation (3.4 MHz, 1 W/cm^2, 50% duty cycle) for 10 minutes. The cells were then washed with PBS and trypsinized for flow cytometry. For CLSM, inside 35 mm glass bottom dishes, CT26 cells were seeded at a density of 1×10^5 cells/mL and treated in the same way as flow cytometry but not detached. The cells were washed with PBS, exchanged with warm phenol-red-free RPMI-1640 medium, and mounted for CLSM immediately using a Leica Stellaris 8 microscope.

AM/PI staining

The general cell death after SDT treatment was evaluated on CT26 by Calcein-AM/Propidium Iodide (PI) staining with CLSM. CT26 cells were seeded at a density of 1×10^5 cells/mL inside 35 mm glass bottom dishes. After overnight culturing, the cells were treated with TBP, Hf-TBP and TBP@MOL at equivalent TBP concentrations of 5 μM and further incubated for 6 hours. Cells were irradiated by US

(3.4 MHz, 1 W/cm^2, 50% duty cycle) for 10 minutes. The cells were further cultured for 24 hours and then stained with Calcein-AM (5 μM) and PI (1 μg/mL) in serum-free RPMI-1640 medium for 30 minutes. The cells were then washed with PBS, exchanged with warm phenol-red-free RPMI-1640 medium, and mounted for CLSM immediately using a Leica Stellaris 8 microscope.

Apoptosis analysis

The apoptosis after SDT treatment was evaluated on CT26 cells by flow cytometry. CT26 cells were seeded at a density of 2×10^5 cells/mL in 6-well plates and the cells were treated with TBP, Hf-TBP and TBP@MOL at equivalent TBP concentrations of 5 μM and further incubated for 4 hours. Then the plates were treated by US irradiation (3.4 MHz, 1 W/cm^2, 50% duty cycle) for 10 minutes. The cells were further incubated for 24 hours, washed with PBS, and trypsinized for the staining of Alexa Fluor 488 Annexin V/dead cell apoptosis kit (Thermo Fisher Scientific, USA) following the vendor's protocol.

1.11. In Vivo Study

In vivo SDT efficacy was tested on subcutaneous CT26 and 4T1 tumor models. BALB/c mice were inoculated with 2×10^6 CT26 or 4T1 cells per mouse subcutaneously onto the right flank. After one week, the mice with tumor volume around 80 mm^3 were randomized for SDT treatment. PBS, TBP, Hf-TBP, MOL, or TBP@MOL was injected intratumorally with an equivalent TBP dose of 0.2 μmol (n = 5) every 2 days. 6 hours later, the mice were anaesthetized with 2% (V/V) isoflurane/O_2 and the tumor was treated by the sonication (3.4 MHz, 2 W/cm^2, 50% duty cycle) for 10 minutes. Tumor sizes were measured with an electronic caliper (tumor volume = length×width^2/2) and body weight was monitored with an electronic scale daily. At day 19, the mice were euthanized, and the tumors were weighed, photographed and sectioned for H&E and TUNEL staining. Major organs were sectioned for hematoxylin-eosin (H&E) staining to evaluate general toxicity.

1.12. Statistical analysis

Statistical analysis for in vivo efficacy was performed on Origin Lab software using One-way Repeated Measures ANOVA method with Tukey's honest significance test. The tumor volume and weight at the last day of experiment were chosen for analysis (n = 5).

2. Supporting Tables

Table S1. IC_{50} values of TBP@MOL, TBP, and Hf-TBP with or without ultrasound irradiation on CT26 cells.

	TBP@MOL	TBP	Hf-TBP
With ultrasound	6.0 μM	40 μM	> 80 μM
Without ultrasound	> 80 μM	> 80 μM	> 80 μM

Table S2. IC_{50} values of TBP@MOL, TBP, and Hf-TBP with or without ultrasound irradiation on 4T1 cells.

	TBP@MOL	TBP	Hf-TBP
With ultrasound	6.1 μM	> 40 μM	> 40 μM
Without ultrasound	> 40 μM	> 40 μM	> 40 μM

Table S3. Fluorescence decay fitting values for the TBP chromophores in TBP@MOL, Hf-TBP and TBP. The table shows values for the fitted fluorescence decay times (τ_i), pre-exponential weighting coefficients (α_i), and chi-squared distribution (χ^2). τ_3 is approximate as it exceeds our 200 ns time window and is not included in calculating τ_{avg}.

Sample	τ_{avg} (ns)	τ_1 (ns)	τ_2 (ns)	τ_3 (μs)	α_1	α_2	α_3	χ^2
TBP@MOL	3.12	1.63	8.13	~50.0	0.77	0.23	0.0016	0.33
Hf-TBP	3.33	2.06	8.19	~42.0	0.78	0.21	0.0009	0.21
TBP	9.52	-	9.52	~35.0	-	1.00	-	0.22

Table S4. Fluorescence decay fitting values for the DBP chromophores in DBP@MOL, Hf-DBP and DBP. The table shows values for the fitted fluorescence decay times (τ_i), pre-exponential weighting coefficients (α_i), and chi-squared distribution (χ^2). τ_3 is approximate as it exceeds our 200 ns time window and is not included in calculating τ_{avg}.

Sample	τ_{avg} (ns)	τ_1 (ns)	τ_2 (ns)	τ_3 (μs)	α_1	α_2	α_3	χ^2
DBP@MOL	4.34	1.49	10.44	~15.4	0.67	0.32	0.002	0.47
Hf-DBP	8.43	0.69	11.01	~13.3	0.25	0.75	0.002	0.47
DBP	11.81	-	11.81	~12.0	-	1.00	0.002	0.21

Table S5. Fluorescence decay fitting values for the DBB-Ir chromophores in TBP@MOL, DBP@MOL and MOL. The table shows values for the fitted fluorescence decay times (τ_i), pre-exponential weighting coefficients (α_i), and chi-squared distribution (χ^2). τ_3 is approximate as it exceeds our 200 ns time window and is not included in calculating τ_{avg}.

Sample	τ_{avg} (ns)	τ_1 (ns)	τ_2 (ns)	τ_3 (μs)	α_1	α_2	α_3	χ^2

TBP@MOL	1.98	0.91	7.06	~20.0	0.78	0.18	0.001	1.04
DBP@MOL	2.11	1.13	6.98	~20.0	0.82	0.17	0.0	0.54
MOL	2.26	0.67	5.7	~12.4	0.57	0.33	0.096	2.36

Table S6. The absorption (negative) feature time constants and their spread. Each time trace in the probe wavelength range were fit with mono-exponentials and the average and standard deviation of the time constants is reported. The lowest and highest values of χ^2 is reported for a given region resulting from fitting all the time traces.

Sample	λ range (nm)	τ_{avg} (ns)	σ_τ (ns)	χ^2 range
Hf-TBP	600-630	1.06	0.02	0.03-0.06
	680-710	1.15	0.09	0.03-0.07
TBP@MOL	540-630	2.10	0.45	0.01-0.04
	680-700	0.63	0.09	0.02-0.04

$$J(\lambda) = \int_0^\infty \epsilon_A(\lambda)\lambda^4 F_D(\lambda)\, d\lambda$$

Equation S1. Spectral overlap integral *J*(λ). λ is the spectrum wavelength, ε_A is the acceptor absorption coefficient, F_D is the donor fluorescence emission normalized to 1.

Table S7. Spectral overlap integrals. $J(\lambda)$ values for TBP and DBP acceptors (A) with MOL (DBB-Ir) donors (D), calculated using a|e – UV-Vis-IR Spectral Software 1.2 (FluorTools, DK).

Donor-acceptor pair	$J(\lambda)$ [nm^4 M^{-1} cm^{-1}]
TBP (*A*) + MOL (*D*)	7.10×10^{14}
DBP (*A*) + MOL (*D*)	5.42×10^{14}
TBP (*A*) + Hf-BTB (*D*)	1.43×10^{15}

Table S8. Tumor growth inhibition (TGI) values for CT26 tumor models at the end-point.

Group	TGI
PBS(-)	0%
PBS(+)	0.6%
TBP(-)	19.8%
TBP(+)	25.1%
Hf-TBP(-)	10%
Hf-TBP(+)	16.7%
MOL(-)	6.7%
MOL(+)	21.9%
TBP@MOL(-)	9.8%
TBP@MOL(+)	87.0%

Table S9. Tumor growth inhibition (TGI) values for 4T1 tumor models at the end-point.

Group	TGI
PBS(+)	5.2 %
TBP(+)	41.5%
Hf-TBP(+)	50.0%
TBP@MOL(+)	82.7%

3. Supporting Figures

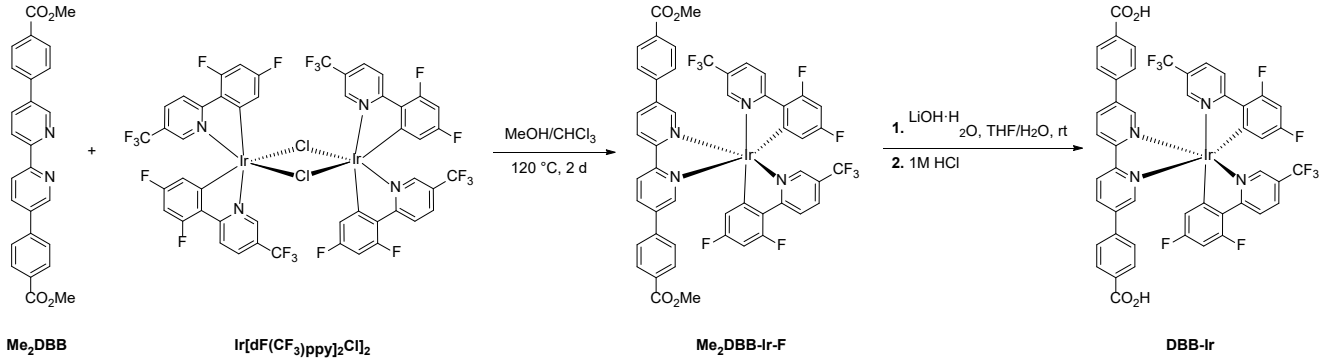

Figure S1. Synthesis of DBB-Ir.

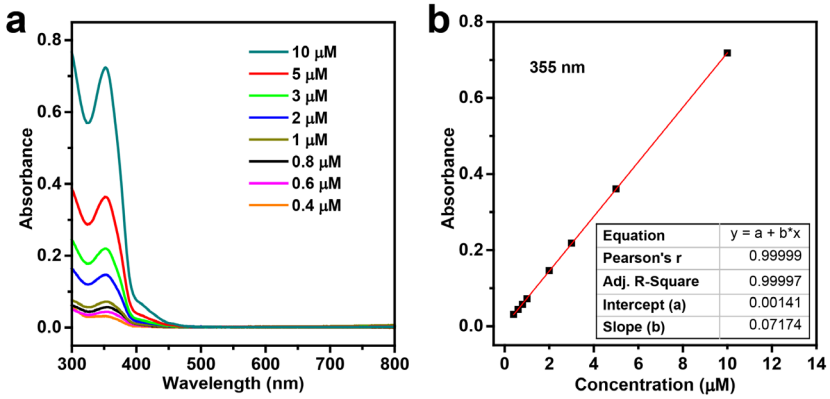

Figure S2. UV-Vis standard curve for DBB-Ir. (a) UV-Vis absorption spectra of DBB-Ir in DMSO at different concentrations. The absorption at 355 nm corresponds to the metal-to-ligand charge transfer (MLCT) transition. (b) Linear fit of the DBB-Ir absorbance at 355 nm as a function of concentration.

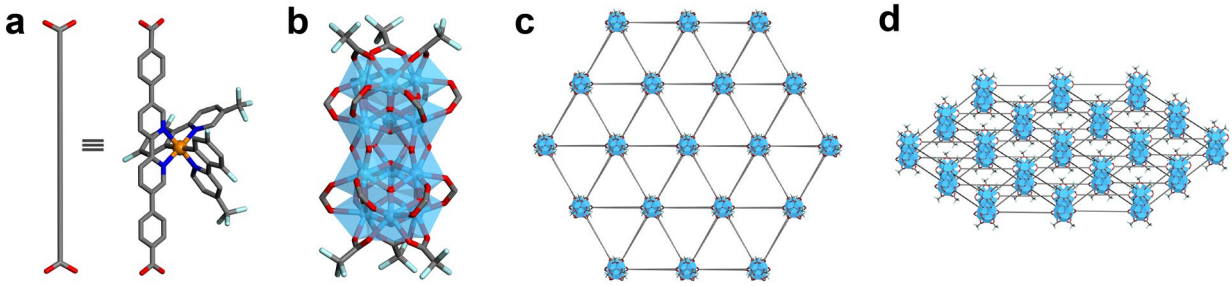

Figure S3. Structure models of the MOL. (a) Simplified (left) and full (right) structure model of bridging ligand DBB-Ir. (b) The structure of SBU $Hf_{12}(\mu_3\text{-}O)_8(\mu_3\text{-}OH)_8(\mu_2\text{-}OH)_6(RCO_2)_{12}(TFA)_6$ [RCO_2 represents the carboxylate group on DBB-Ir]. (c) A view along the *c* axis of the MOL showing its monolayer morphology. (d) Side view of the MOL showing the positions of the bridging DBB-Ir ligands within the monolayered framework (orange: Ir, sky blue: Hf, pale light blue: F, red: O, blue: N, grey: C; H atoms are omitted for clarity).

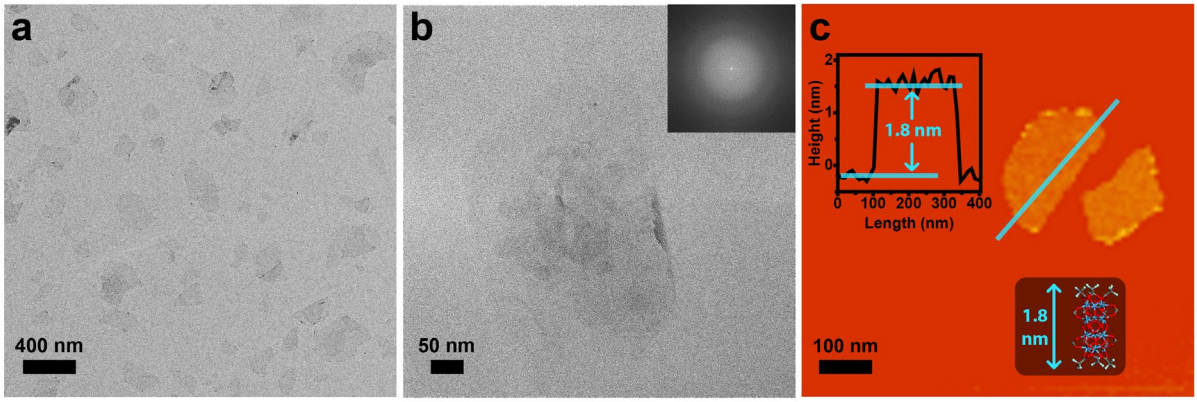

Figure S4. Morphological characterization of the MOL. (a) TEM image of the MOL. (b) HR-TEM image of the MOL with its FFT (inset). (c) AFM topographic image, measured height profile (inset, left) and modeled height (inset, bottom) of the MOL.

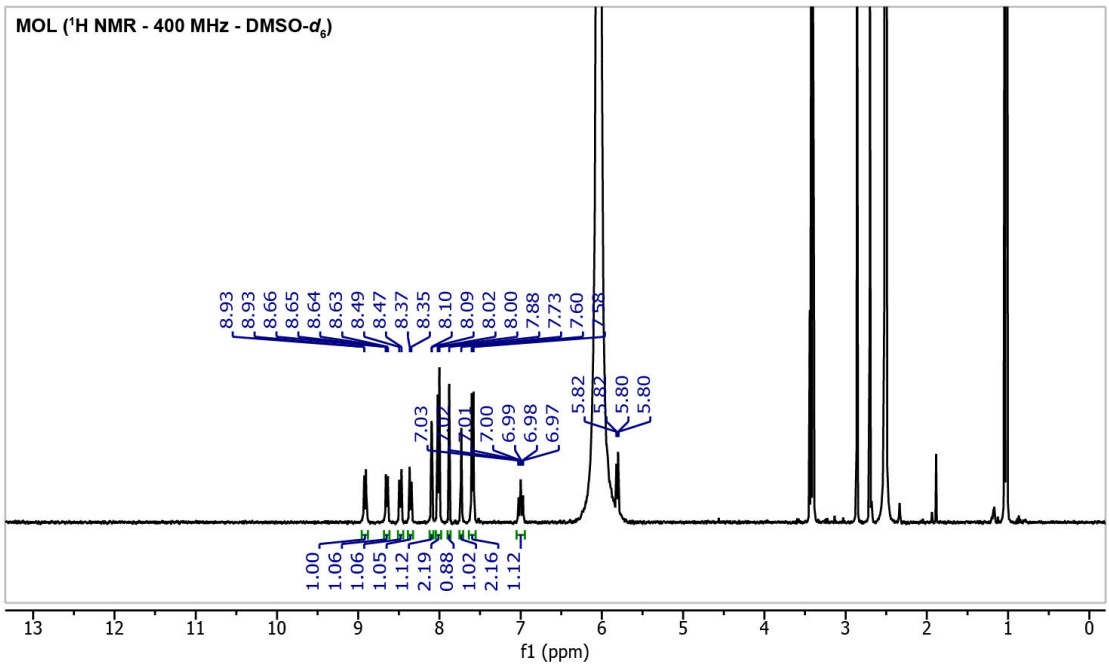

Figure S5. ^{1}H NMR spectrum of the digested MOL.

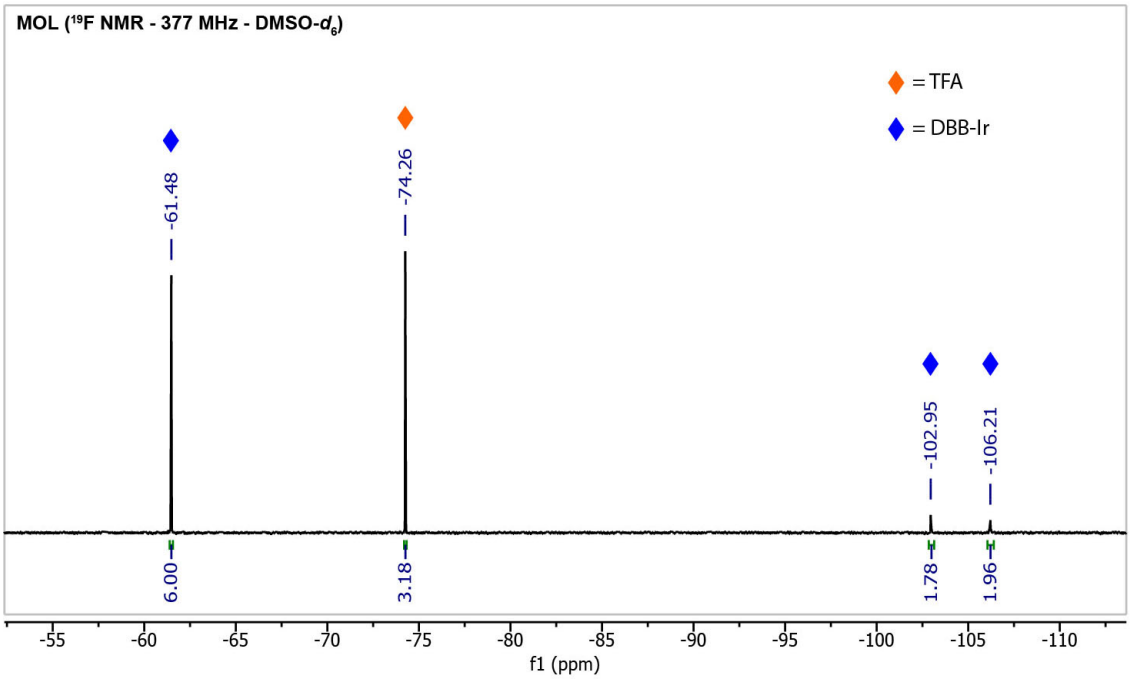

Figure S6. ^{19}F NMR spectrum of the digested MOL.

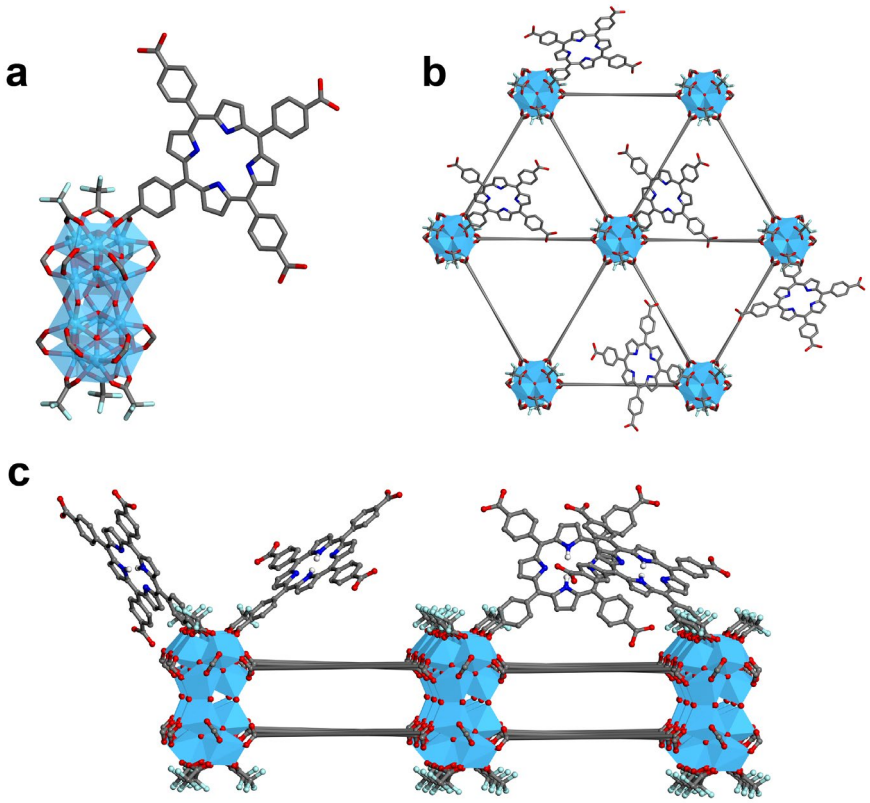

Figure S7. Structure models of TBP@MOL. (a) The structure of monosubstituted SBU $Hf_{12}(\mu_3\text{-}O)_8(\mu_3\text{-}OH)_8(\mu_2\text{-}OH)_6(\mu_2\text{-}RCO_2)_{12}(\mu_2\text{-}TFA)_5(TBP)$ [RCO_2 represents the carboxylate group on DBB-Ir]. (b) A view along the *c* axis of TBP@MOL showing its monolayer morphology. (c) Side view of TBP@MOL showing SBU-anchored TBP sensitizers. Although not shown here, TBP can replace TFA on the top or bottom of the SBU (sky blue: Hf, pale light blue: F, red: O, blue: N, grey: C; H atoms are omitted for clarity).

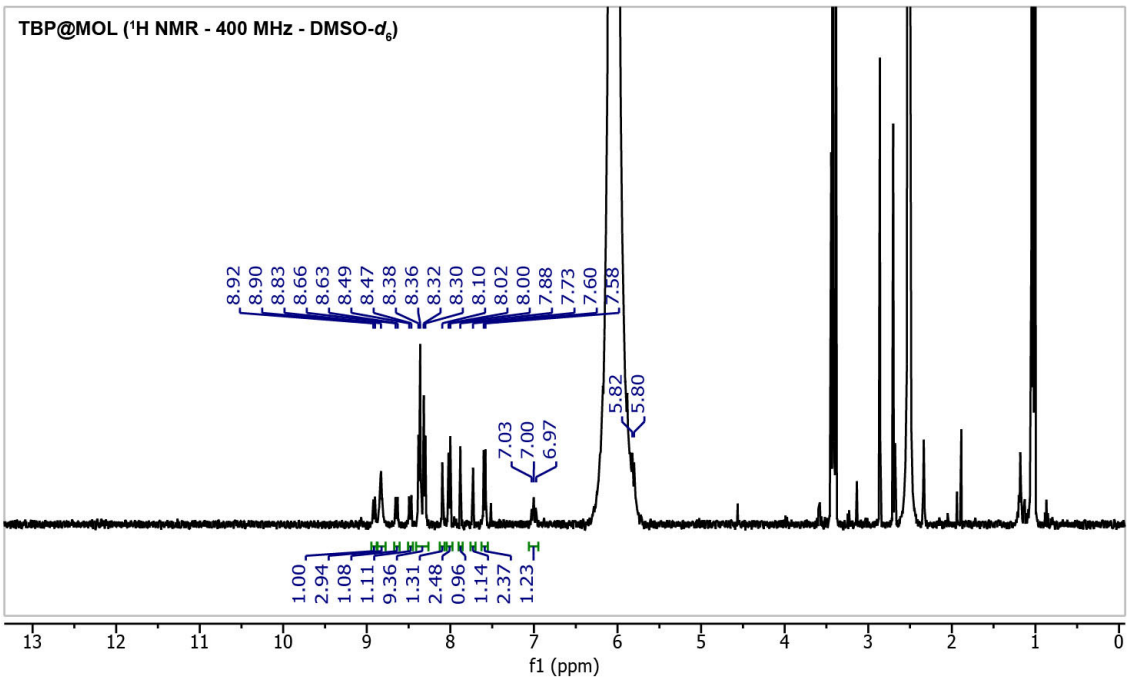

Figure S8. ^{1}H NMR spectrum of TBP@MOL.

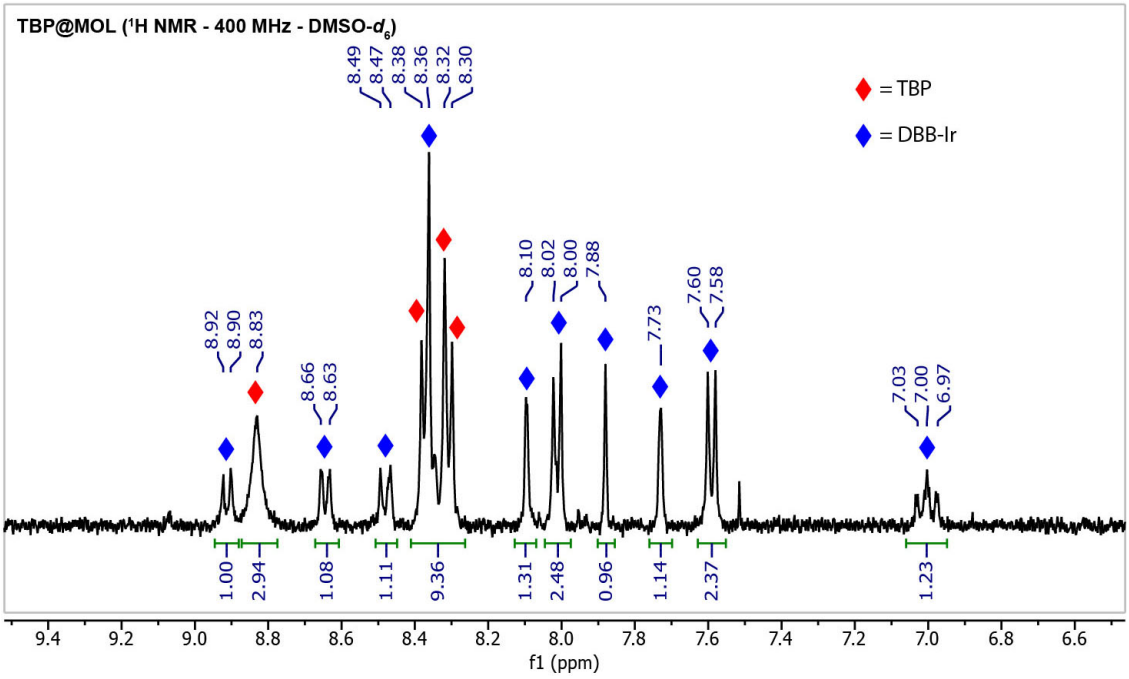

Figure S9. Aromatic region of the ^{1}H NMR spectrum of digested TBP@MOL. Digested TBP@MOL in DMSO-d_6 shows the characteristic peaks of both TBP and DBB-Ir.

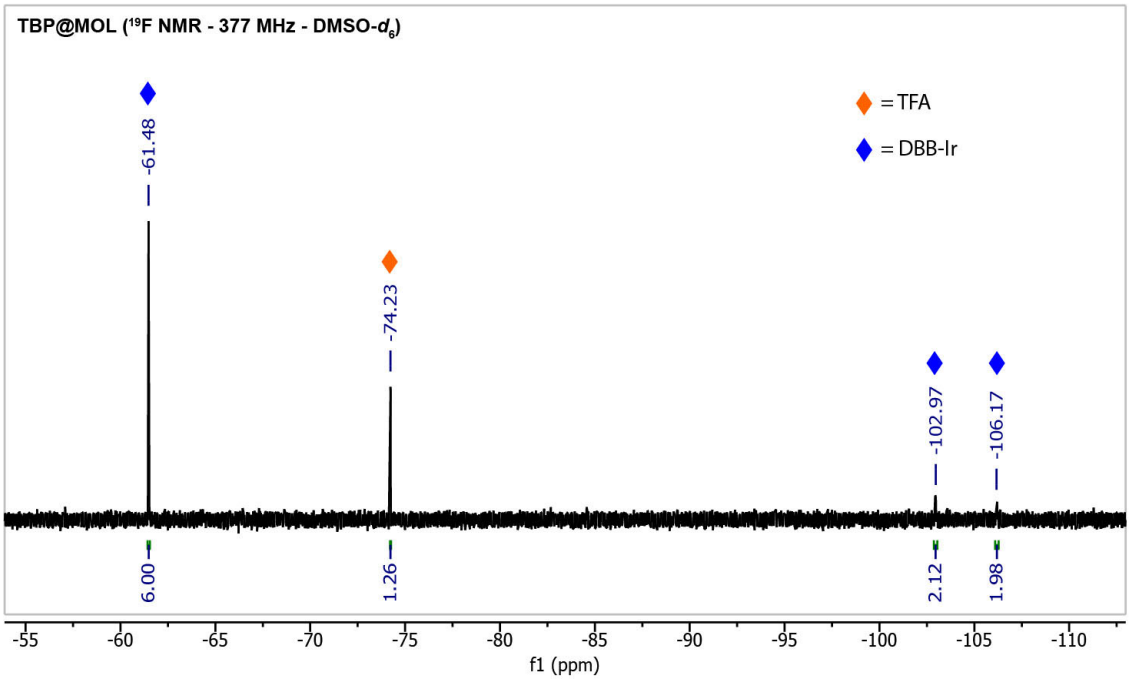

Figure S10. ^{19}F NMR spectrum of digested TBP@MOL. Digested TBP@MOL in DMSO-d_6 shows a reduction in the DBB-Ir to TFA integrated signal ratio, suggesting partial carboxylate exchange of TFA with TBP on the Hf_{12} SBUs.

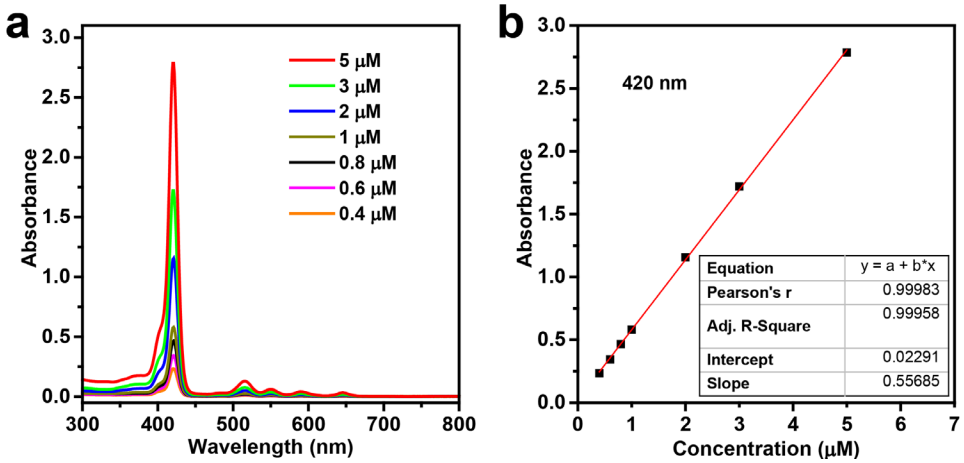

Figure S11. UV-Vis standard curve for TBP. (a) UV-Vis absorption spectra of TBP in DMSO at different concentrations. (b) Linear fit of the TBP absorbance at 420 nm as a function of concentration.

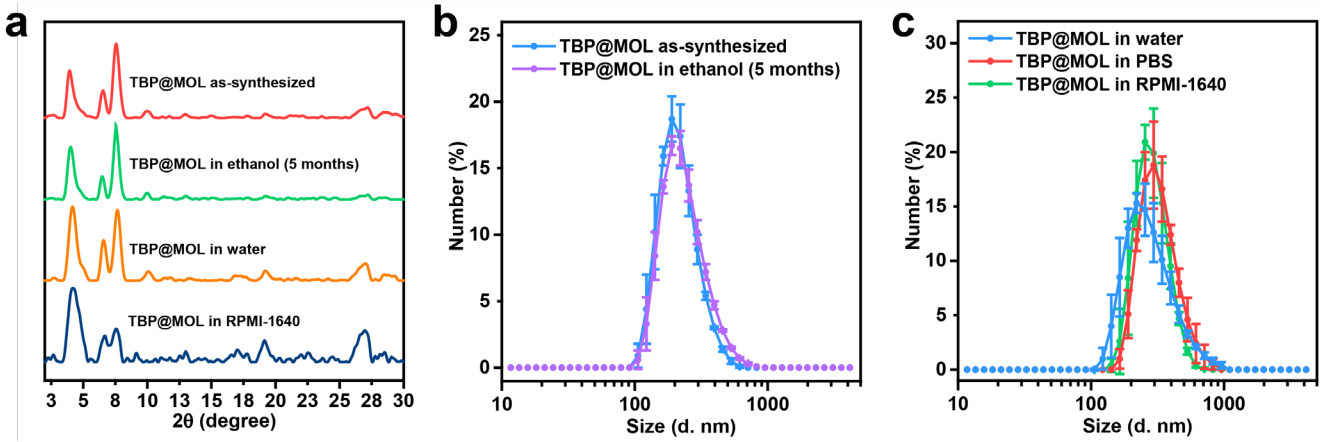

Figure S12. Stability of TBP@MOL in different media. (a) PXRD patterns of TBP@MOL freshly prepared (as-synthesized), stored in ethanol for 5 months at room temperature, incubated in water for 24 hours at room temperature, and incubated in RPMI-1640 medium for 6 hours at 37 °C. (b) Number-averaged diameters of TBP@MOL freshly prepared and stored in ethanol for 5 months at room temperature. The final dispersions were prepared in ethanol. (c) Number-averaged diameters of TBP@MOL incubated in water for 24 hours at room temperature, in PBS for 24 hours at room temperature, and in RPMI-1640 medium for 6 hours at 37 °C. The final dispersions were prepared in water.

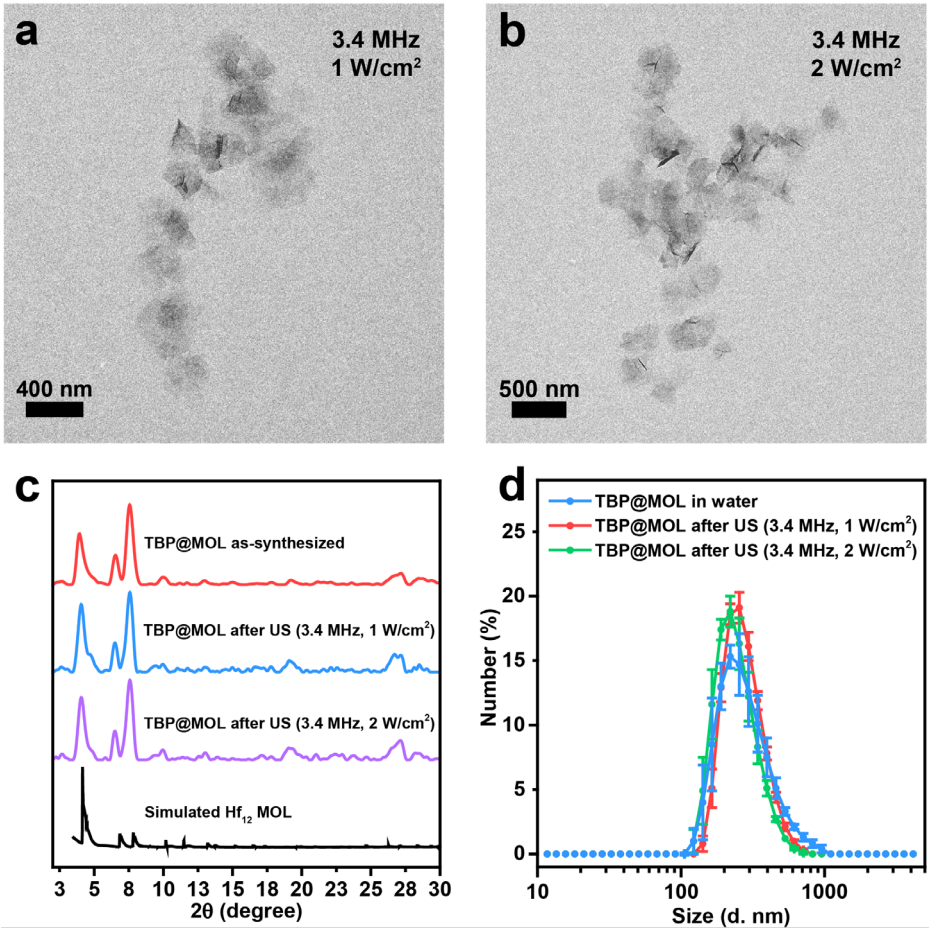

Figure S13. Stability of TBP@MOL after US irradiation. TEM images of TBP@MOL after US irradiation, with 3.4 MHz frequency and either (a) 1 W/cm^2 or (b) 2 W/cm^2 power density, for 10 minutes in water. (b) PXRD patterns of TBP@MOL before and after US irradiation, with 3.4 MHz frequency

and either 1 W/cm^2 or 2 W/cm^2 power density, for 10 minutes in water. (d) Number-averaged diameters of TBP@MOL before and after US irradiation, with 3.4 MHz frequency and either 1 W/cm^2 or 2 W/cm^2 power density, for 10 minutes in water. The final dispersions are prepared in water. Although the crystallinity of TBP@MOL is retained, shock waves induced by ultrasound lead to interparticle collisions that slightly affect the crystallinity of the particles. However, due to their nanoscale size, they do not have sufficient collisional energy to fuse or agglomerate.[8]

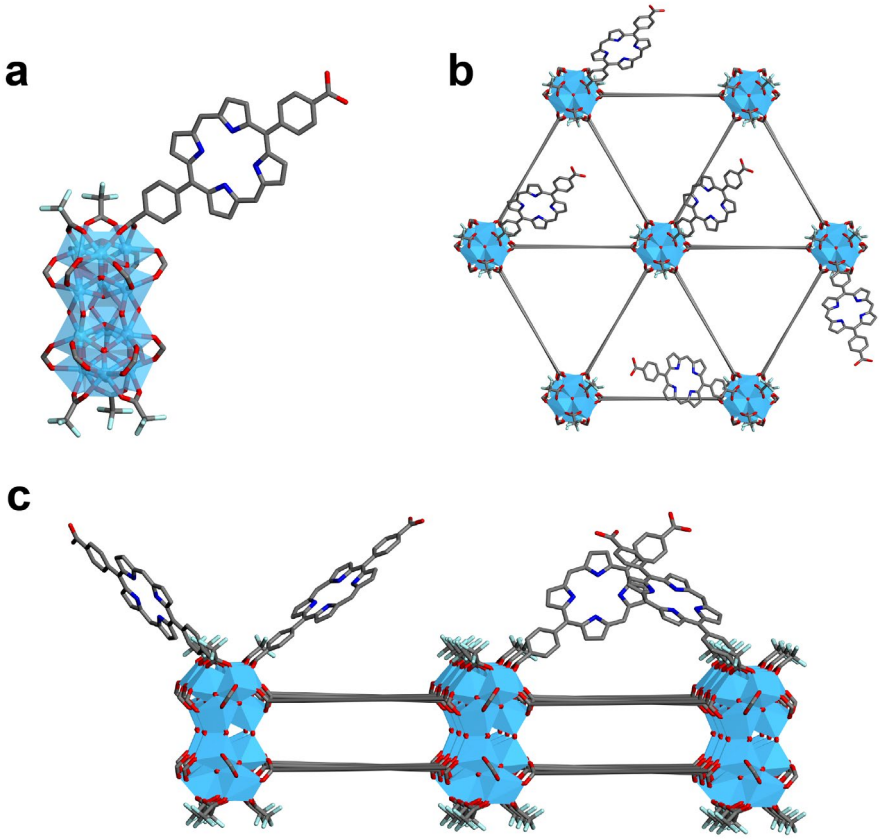

Figure S14. Structure models of DBP@MOL. (a) The structure of monosubstituted SBU $Hf_{12}(\mu_3\text{-}O)_8(\mu_3\text{-}OH)_8(\mu_2\text{-}OH)_6(\mu_2\text{-}RCO_2)_{12}(\mu_2\text{-}TFA)_5$(DBP) [$RCO_2$ represents the carboxylate group on DBB-Ir]. (b) A view along the *c* axis of DBP@MOL showing its monolayer morphology. (c) Side view of DBP@MOL showing the surface-anchored DBP sensitizers on the SBUs. Although not shown here, DBP can be exchanged with TFA on the top or bottom of the SBU (sky blue: Hf, pale light blue: F, red: O, blue: N, grey: C; H atoms are omitted for clarity).

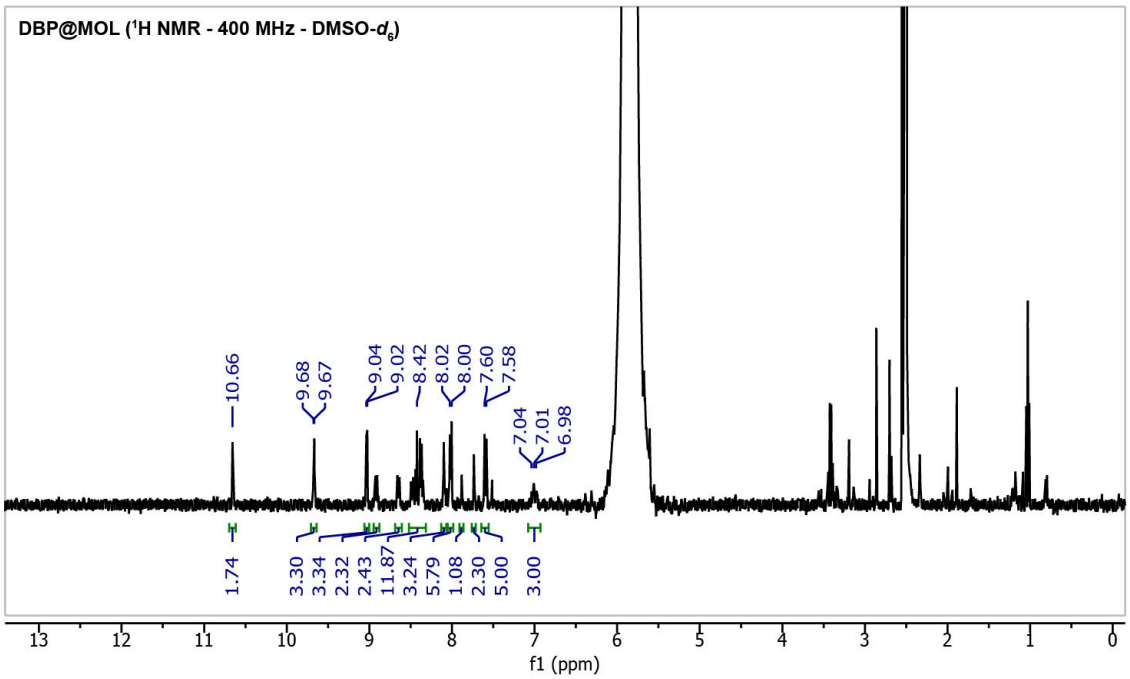

Figure S15. ^{1}H NMR spectrum of DBP@MOL.

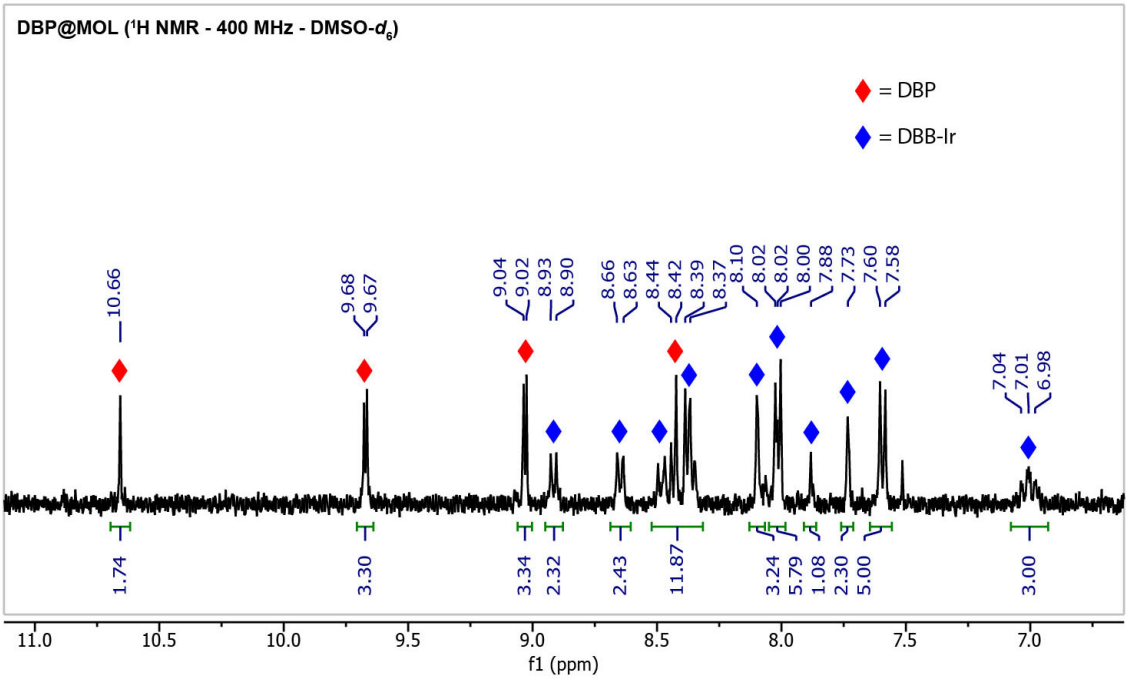

Figure S16. Aromatic region of the ^{1}H NMR spectrum of DBP@MOL. Digested DBP@MOL in DMSO-d_6 shows the characteristic peaks of both DBP and DBB-Ir.

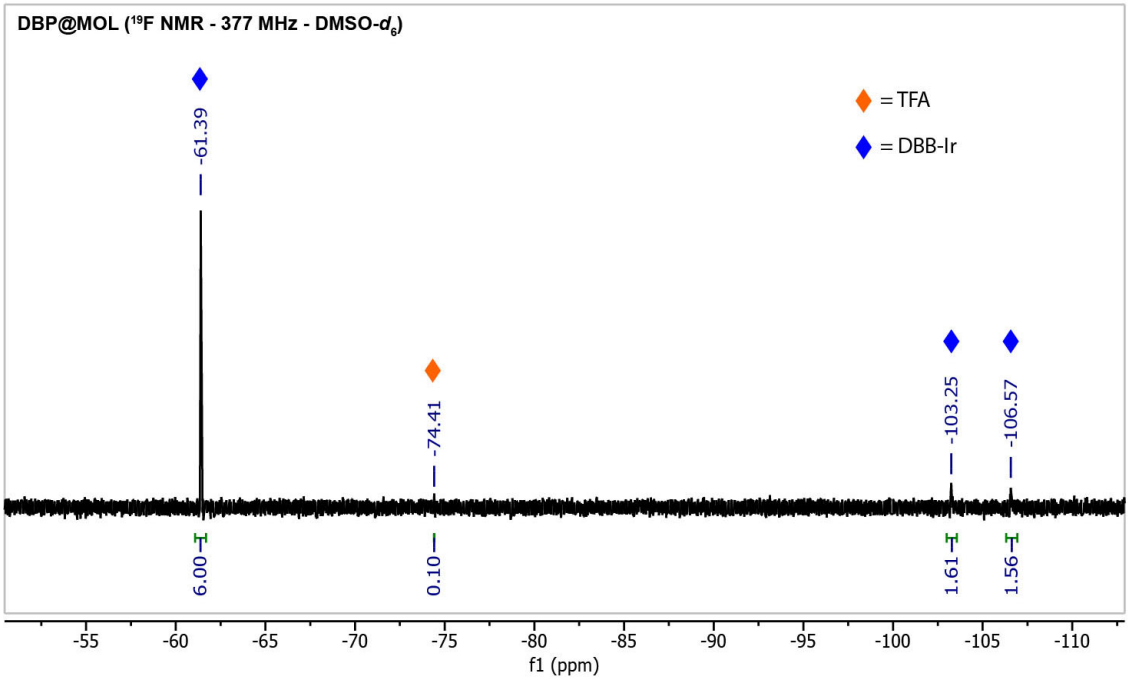

Figure S17. ^{19}F NMR spectrum of DBP@MOL. Digested DBP@MOL in DMSO-d_6 shows almost complete reduction of the DBB-Ir to TFA integrated signal ratio, suggesting nearly complete carboxylate exchange of TFA with DBP on the Hf_{12} SBUs.

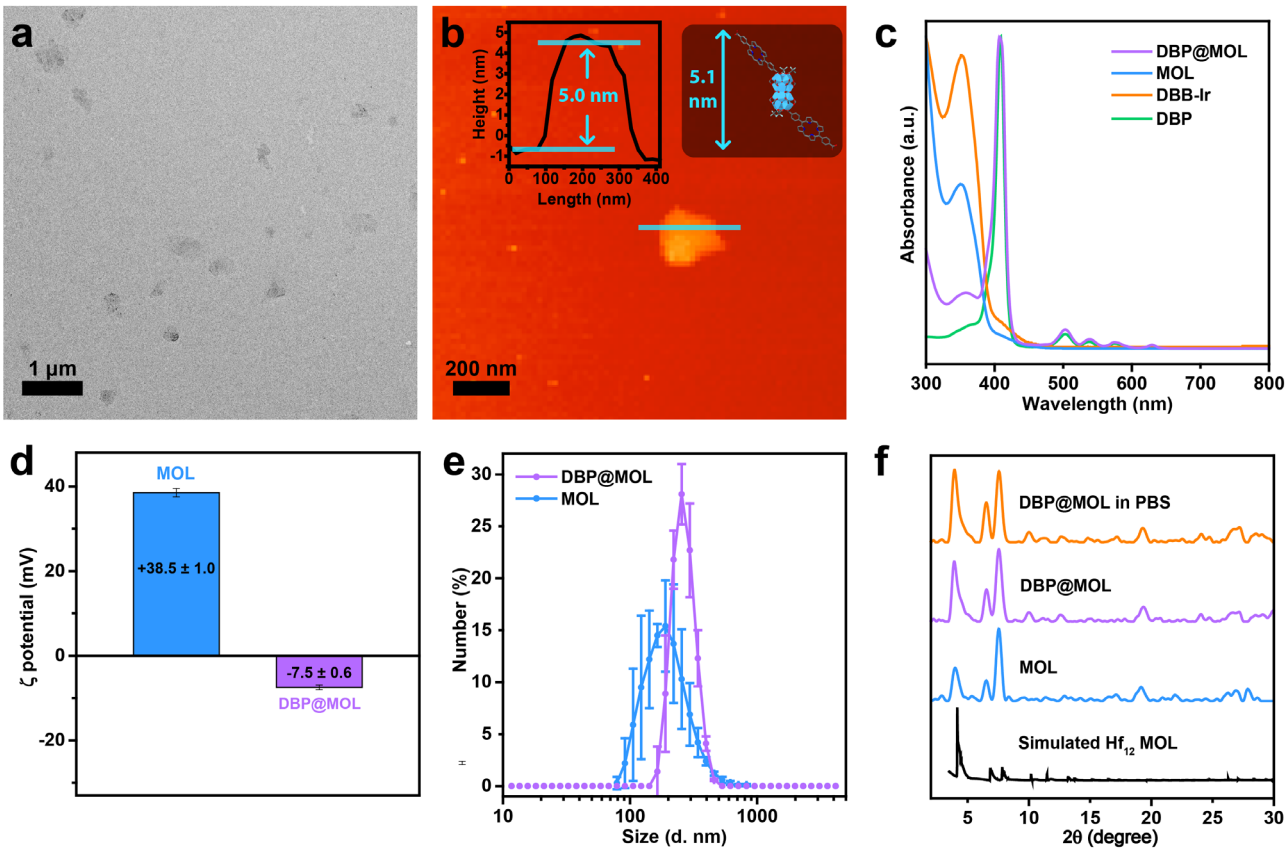

Figure S18. Characterization of DBP@MOL. (a) TEM image of DBP@MOL. (b) AFM topographic image, measured height profile (inset, left) and modeled height (inset, right) of DBP@MOL. (c) Normalized UV-Vis spectra of DBP@MOL and MOL showing the characteristic absorption peaks corresponding to DBP and DBB-Ir. (d) Zeta (ζ) potentials of MOL and DBP@MOL in water. Reversal

of zeta potential is indicative of surface loading of anionic DBP groups to the cationic MOL. (e) Number-averaged diameters for ethanol dispersions of MOL and DBP@MOL, measured by DLS. (f) PXRD patterns of MOL, DBP@MOL as synthesized, DBP@MOL soaked in PBS for 24 hours, and simulated Hf_{12} MOL.

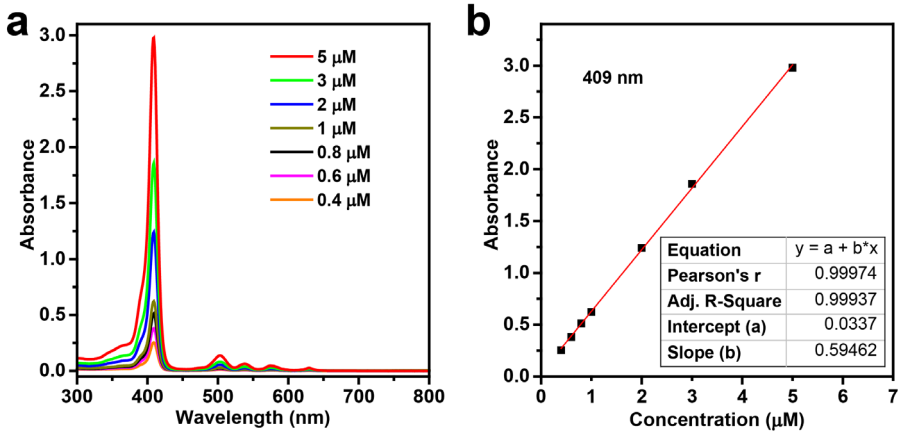

Figure S19. UV-Vis standard curve for DBP. (a) UV-Vis absorption spectra of DBP in DMSO at different concentrations. (b) Linear fit of the DBP absorbance at 409 nm as a function of concentration.

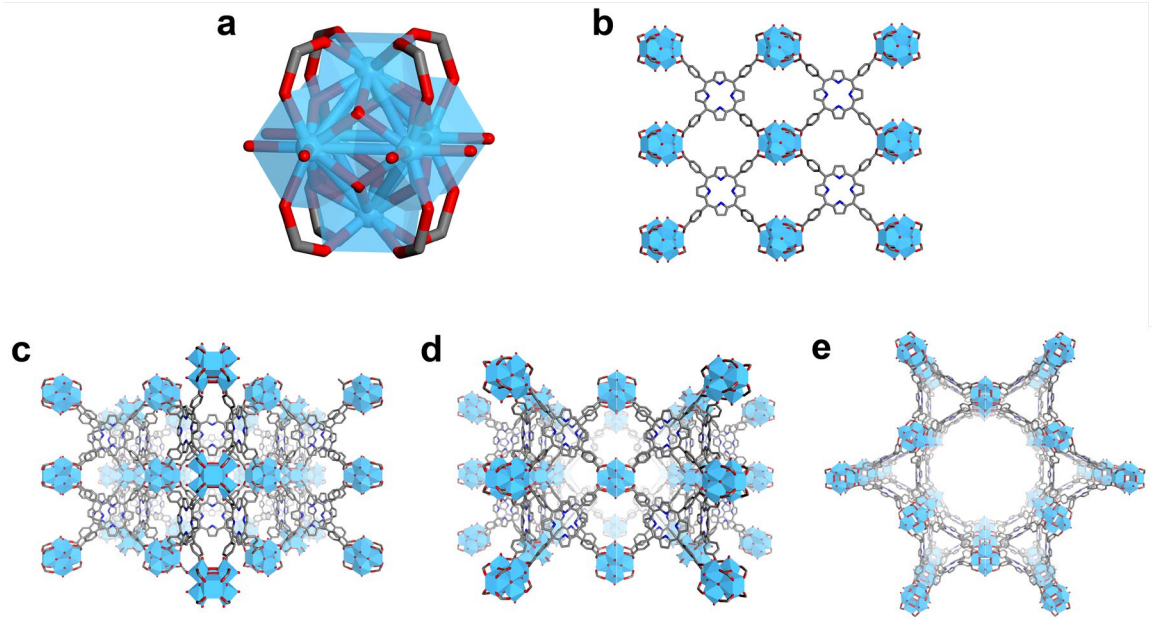

Figure S20. Structure models of Hf-TBP MOF. (a) The structure of SBU $Hf_6(\mu_3\text{-}O)_4(\mu_3\text{-}OH)_4(OH)_4(H_2O)_4(RCO_2)_8$ [RCO_2 represents the carboxylate group on TBP]. (b) View of the [200] plane of Hf-TBP showing the coordination of each TBP to four Hf_6 clusters. Models of Hf-TBP as viewed along the (c) *a* axis, (d) *b* axis, and (e) *c* axis (sky blue: Hf, pale light blue: F, red: O, blue: N, grey: C; H atoms are omitted for clarity).

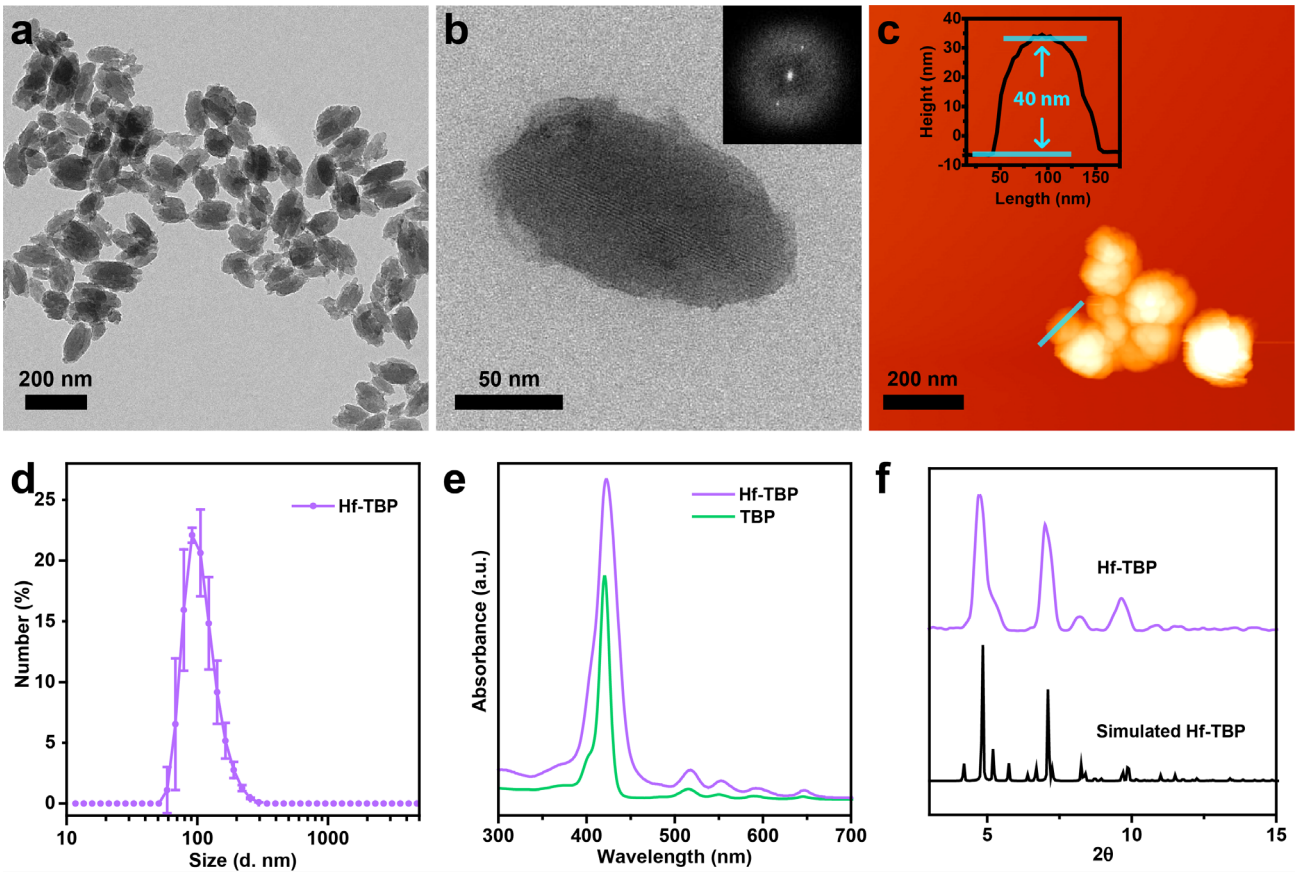

Figure S21. Characterization of Hf-TBP MOF. (a) TEM image of Hf-TBP. (b) HR-TEM image of Hf-TBP with its FFT (inset). (c) Number-averaged diameters of an ethanol dispersion of Hf-TBP measured by DLS. (d) Normalized UV-Vis absorption spectra of Hf-TBP and TBP. (e) PXRD pattern of Hf-TBP and the simulated pattern of Hf-TBP.

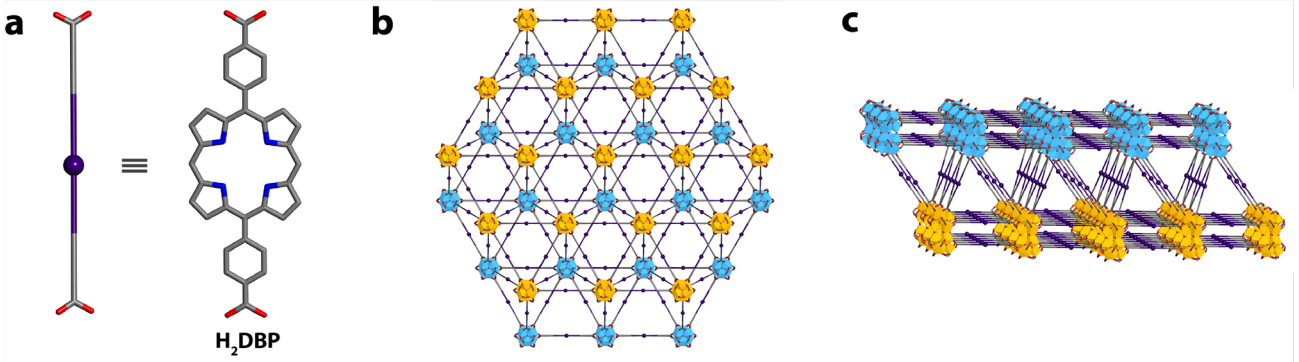

Figure S22. Structure models of Hf-DBP MOF. (a) Simplified (left) and full (right) structure model of bridging ligand DBP. (b) View along the *c* axis of Hf-DBP MOF showing two layers: top layer (blue) and bottom layer (orange). (c) Side view of Hf-DBP MOF showing its multi-layer morphology.

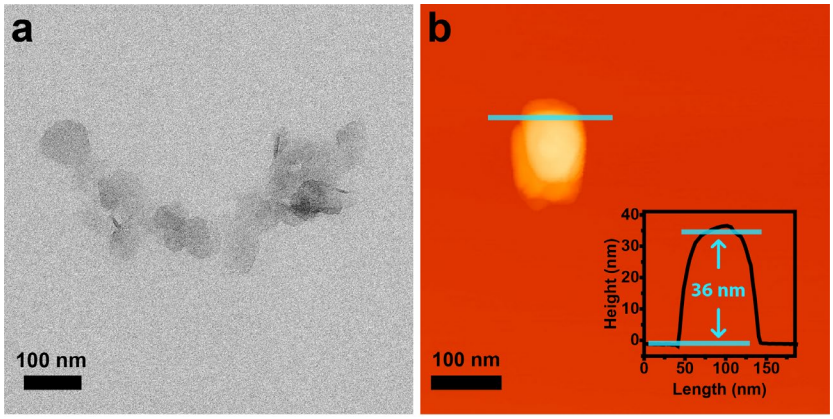

Figure S23. Morphological characterization of Hf-DBP MOF. (a) TEM image of Hf-DBP MOF. (b) AFM topographic image and measured height profile (inset) of Hf-DBP MOF.

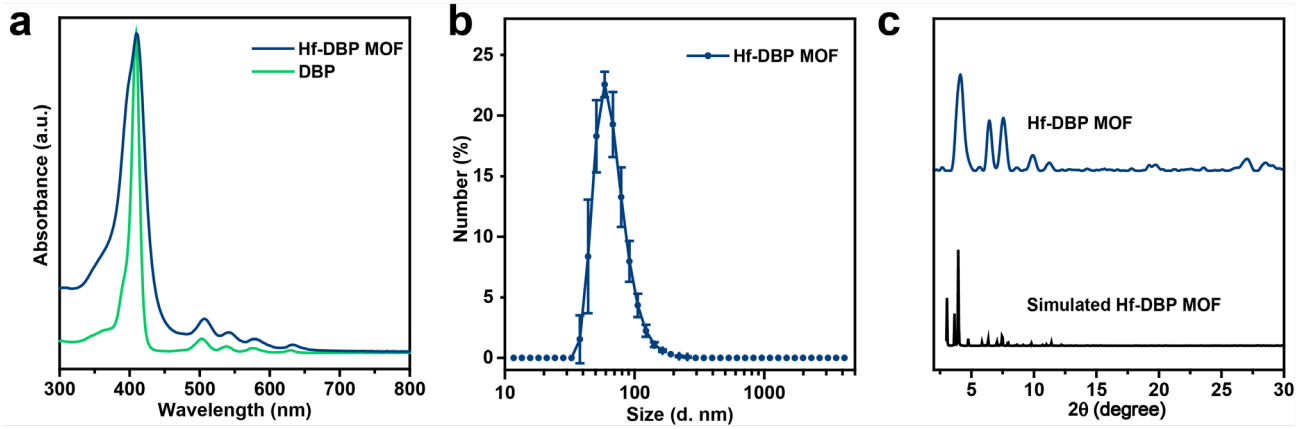

Figure S24. Characterization of Hf-DBP MOF. (a) Normalized UV-Vis spectra of Hf-DBP MOF showing the characteristic absorption peaks corresponding to DBP. (b) Number-averaged diameters for ethanol dispersions of Hf-DBP MOF, measured by DLS. (c) PXRD patterns of Hf-DBP MOF and simulated Hf-DBP MOF.

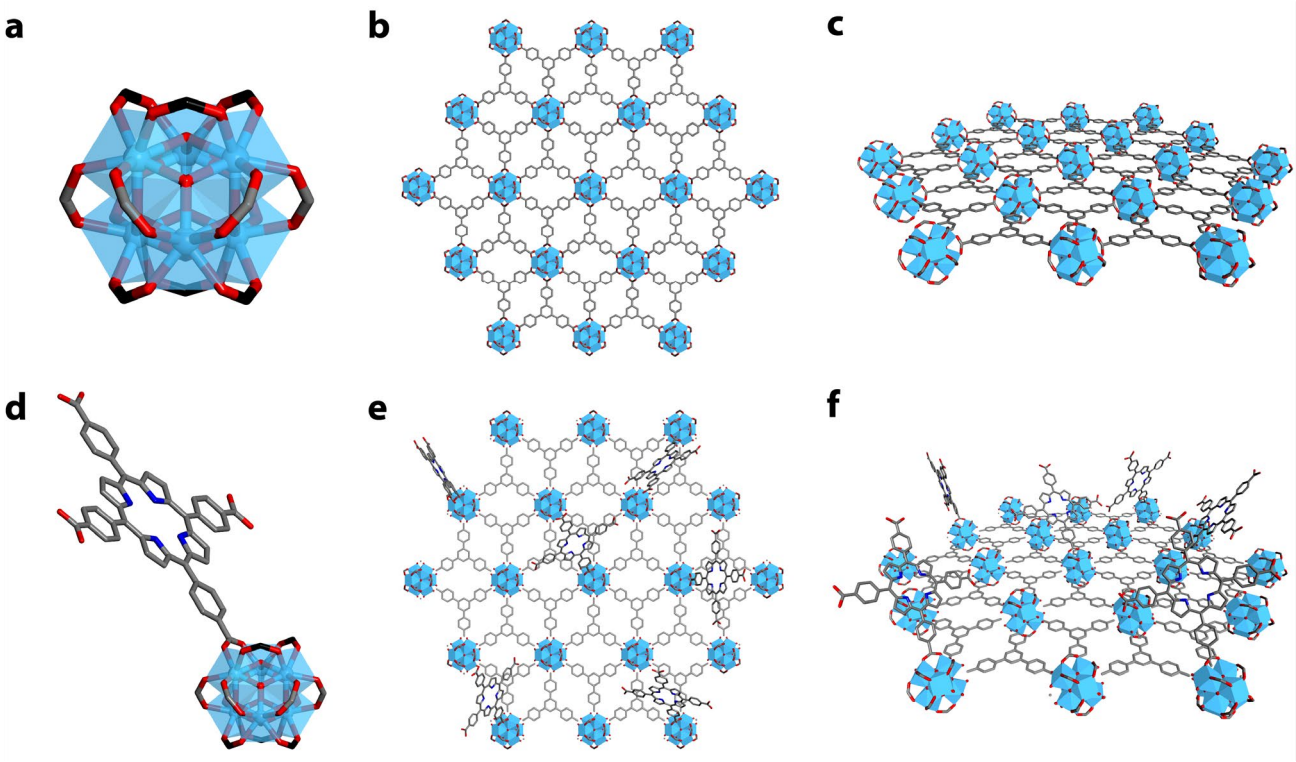

Figure S25. Structure models of Hf-BTB and TBP@Hf-BTB. (a) The structure of SBU $Hf_6(\mu_3\text{-}O)_4(\mu_3\text{-}OH)_4(\mu_2\text{-}FA)_6(\mu_2\text{-}RCO_2)_6$ in Hf-BTB [black atoms represent the carbon on FA; RCO_2 represents the carboxylate group on BTB]. (b) View along the *c* axis of Hf-BTB. (c) Side view of Hf-BTB showing its monolayer morphology. (d) The structure of a monosubstituted SBU $Hf_6(\mu_3\text{-}O)_4(\mu_3\text{-}OH)_4(\mu_2\text{-}FA)_6(\mu_2\text{-}RCO_2)_6(TBP)_1$ in TBP@Hf-BTB. (e) View along the *c* axis of TBP@Hf-BTB. (f) Side view of TBP@Hf-BTB showing its monolayer morphology and surface-anchored TBP. (sky blue: Hf, red: O, blue: N, black/grey: C; H atoms are omitted for clarity).

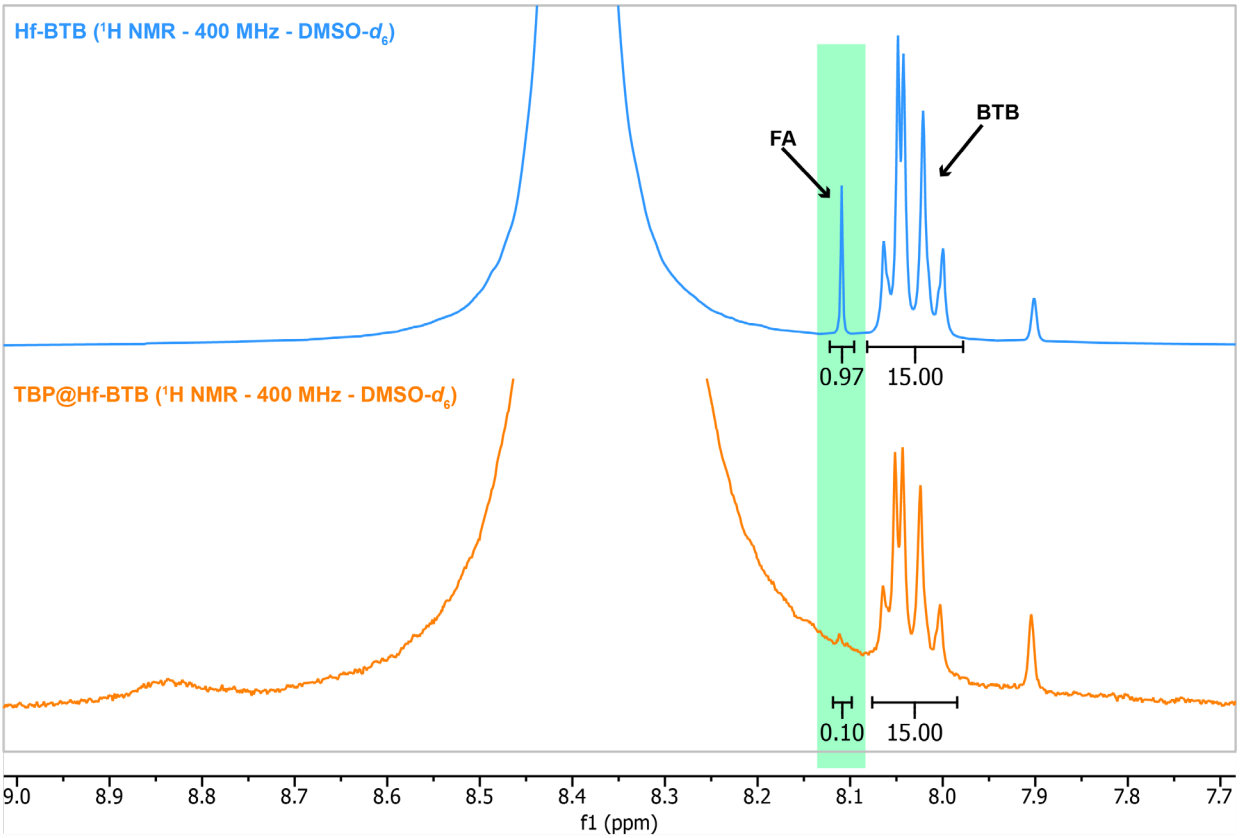

Figure S26. ^{1}H NMR spectra of digested Hf-BTB and TBP@Hf-BTB. The reduction of the FA (δ = 8.12 ppm) to BTB (δ = 8.07-8.00 ppm) integrated signal ratio from Hf-BTB (top) to TBP@Hf-BTB (bottom) is indicative of the carboxylate exchange of FA with TBP on the Hf_6 SBUs.

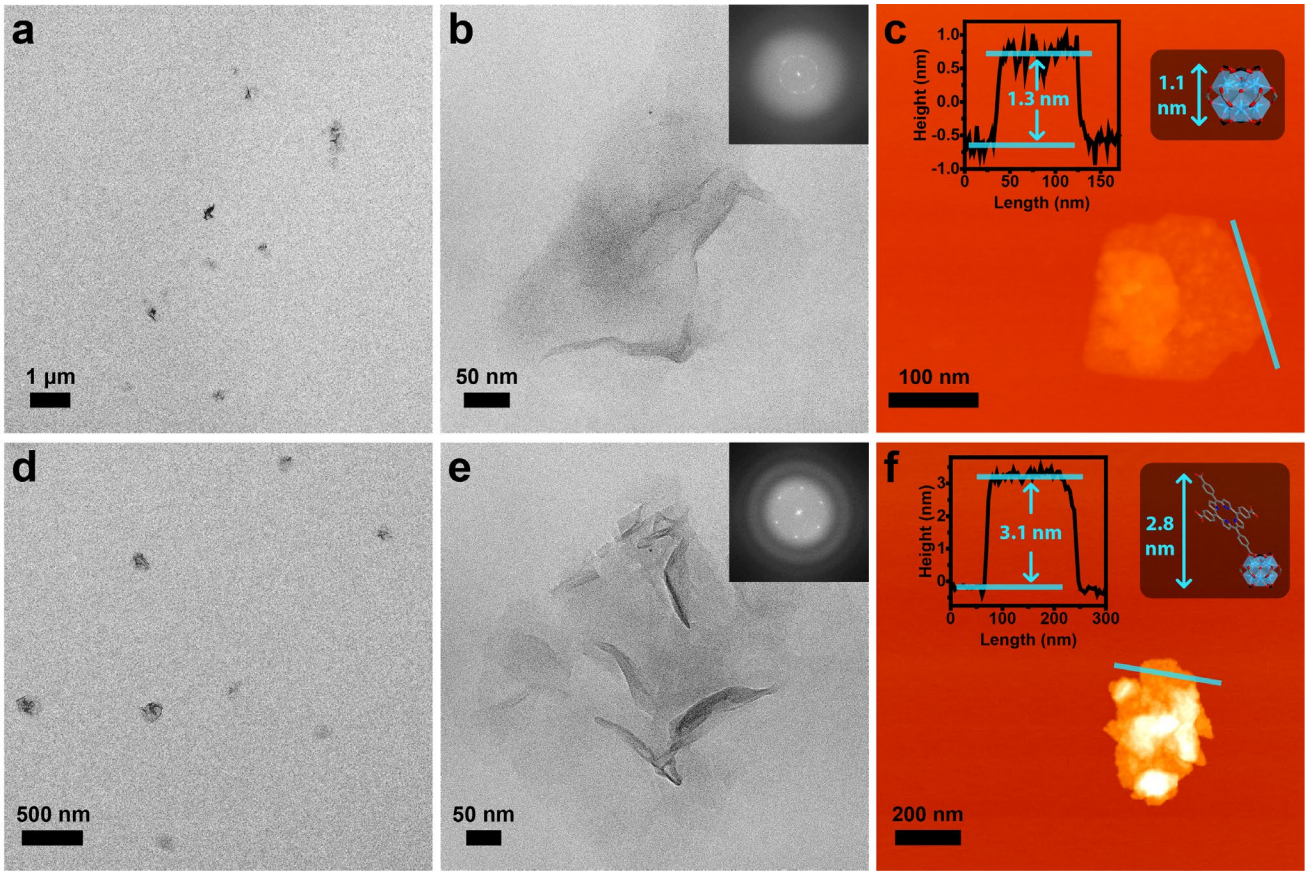

Figure S27. Morphological characterization of Hf-BTB and TBP@Hf-BTB. (a) TEM image of Hf-BTB. (b) HR-TEM image of Hf-TBP with its FFT (inset). (c) AFM topographic image, measured height profile (inset, left) and modeled height (inset, right) of formic acid-capped Hf-BTB. (d) TEM image of TBP@Hf-BTB. (e) HR-TEM image of TBP@Hf-BTB with its FFT (inset). (f) AFM topographic image, measured height profile (inset, left) and modeled height (inset, right) of TBP@Hf-BTB.

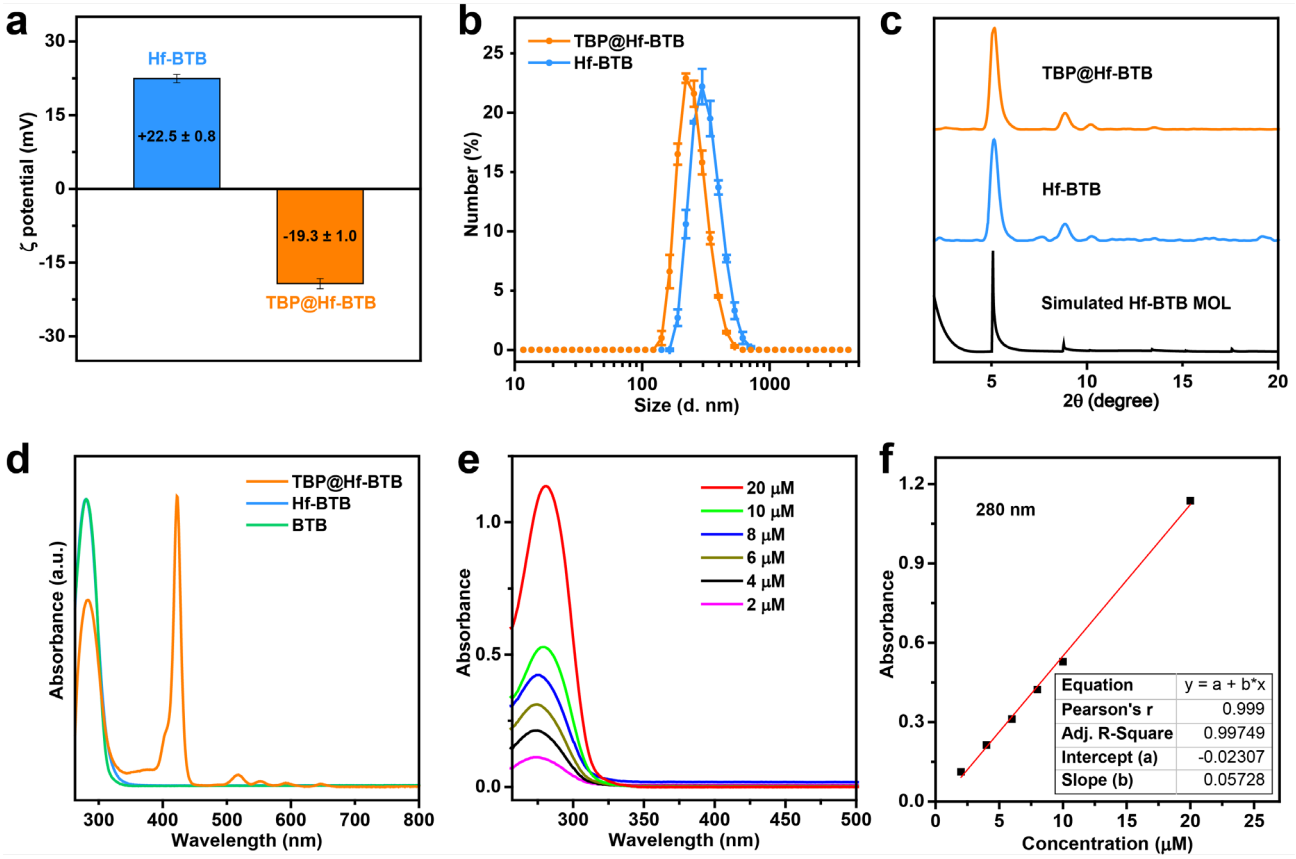

Figure S28. Characterization of Hf-BTB and TBP@Hf-BTB. (a) Zeta (ζ) potentials of Hf-BTB and TBP@Hf-BTB in water. Reversal of zeta potential is indicative of surface loading of anionic TBP groups to Hf-BTB. (b) Number-averaged diameters for ethanol dispersions of TBP@Hf-BTB and Hf-BTB, measured by DLS. (c) PXRD patterns of TBP@Hf-BTB, Hf-BTB, and simulated Hf-BTB MOL. (d) Normalized UV-Vis spectra of TBP@Hf-BTB and Hf-BTB showing the characteristic absorption peaks corresponding to BTB. (e) UV-Vis absorption spectra of BTB in DMSO at different concentrations. (f) Linear fit of the BTB absorbance at 280 nm as a function of concentration.

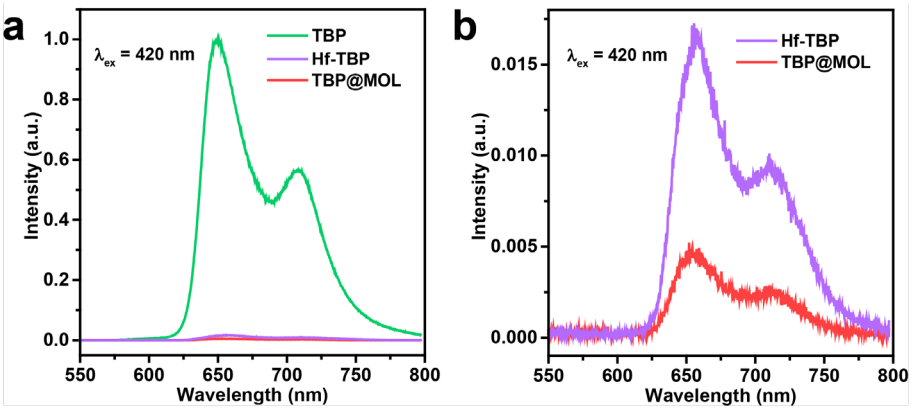

Figure S29. Normalized fluorescence emission spectra of TBP in the TBP systems. (a) Full view and (b) zoomed in view of the fluorescence spectra for TBP, Hf-TBP and TBP@MOL in water at equivalent TBP concentrations of 0.2 μM (λ_{ex} = 420 nm, 3 nm excitation/emission slit widths, 0.1 s integration).

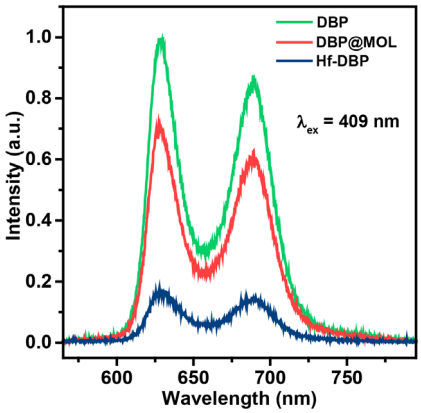

Figure S30. Normalized fluorescence emission spectra of DBP in the DBP systems. Fluorescence spectra for DBP, Hf-DBP, and DBP@MOL in water at equivalent DBP concentrations of 0.2 μM (λ_{ex} = 409 nm, 3 nm excitation/emission slit widths, 0.1 s integration).

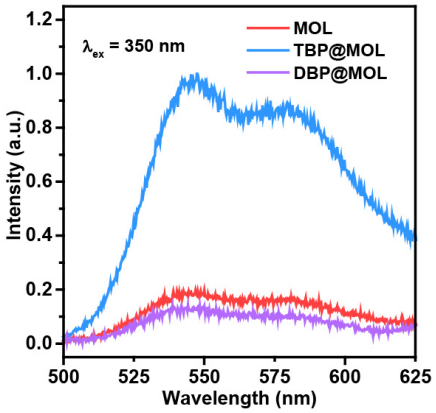

Figure S31. Normalized fluorescence emission spectra of DBB-Ir in the MOL systems. Fluorescence spectra for MOL, TBP@MOL, and DBP@MOL in water at equivalent DBB-Ir concentrations of 0.2 μM (λ_{ex} = 350 nm, 3 nm excitation/emission slit widths, 0.1 s integration).

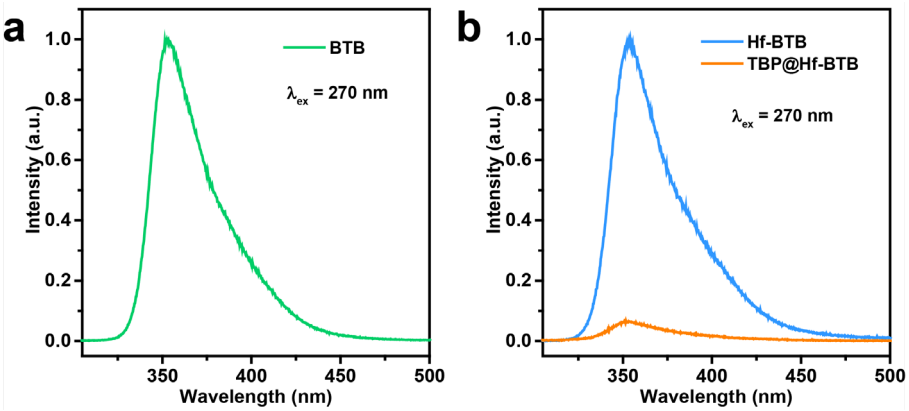

Figure S32. Normalized fluorescence emission spectra of BTB in the BTB systems. Fluorescence spectra of (a) BTB (λ_{ex} = 270 nm, 3 nm excitation/emission slit widths, 0.2 s integration), (b) Hf-BTB, and TBP@Hf-BTB in water at equivalent BTB concentrations of 1 μM (λ_{ex} = 270 nm, 3 nm excitation/emission slit widths, 3.0 s integration).

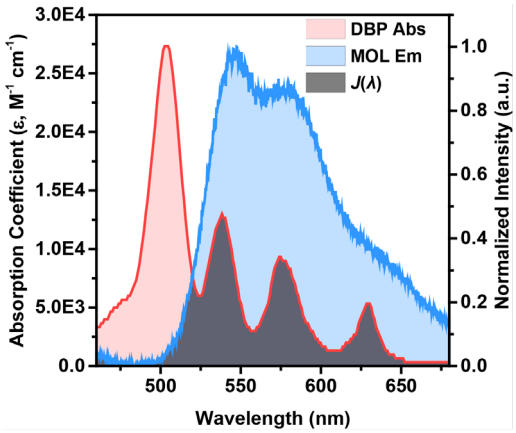

Figure S33. Donor-acceptor absorption and emission spectra of the MOL systems. Absorption spectrum of DBP (acceptor), normalized emission spectrum of MOL (DBB-Ir; donor), and spectral overlap integral $J(\lambda)$.

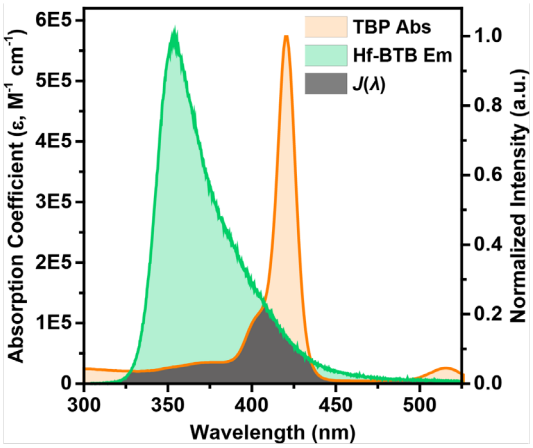

Figure S34. Donor-acceptor absorption and emission spectra of the Hf-BTB system. (a) Absorption spectrum of TBP (acceptor), normalized emission spectrum of Hf-BTB (BTB; donor), and spectral overlap integral $J(\lambda)$.

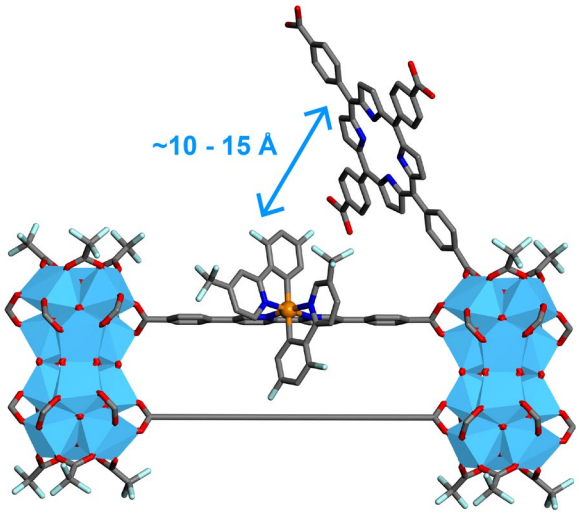

Figure S35. Simulated distance between TBP acceptor and DBB-Ir donor in TBP@MOL.

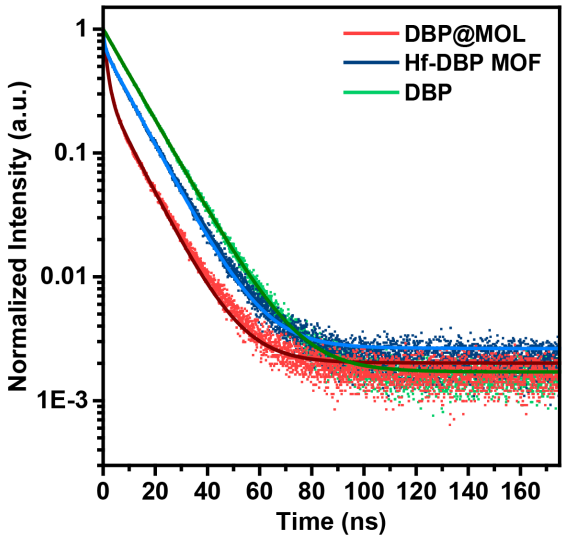

Figure S36. Fluorescence decays of the DBP chromophores using time-correlated single photon counting (TCSPC). Fluorescence decay curves of the DBP chromophore in water dispersions of DBP@MOL, Hf-DBP MOF, and DBP at equivalent DBP concentrations of 0.2 μM (λ_{ex} = 403 nm, λ_{em} = 642 ± 10 nm). Solid lines represent the fits of the correspondingly colored data points.

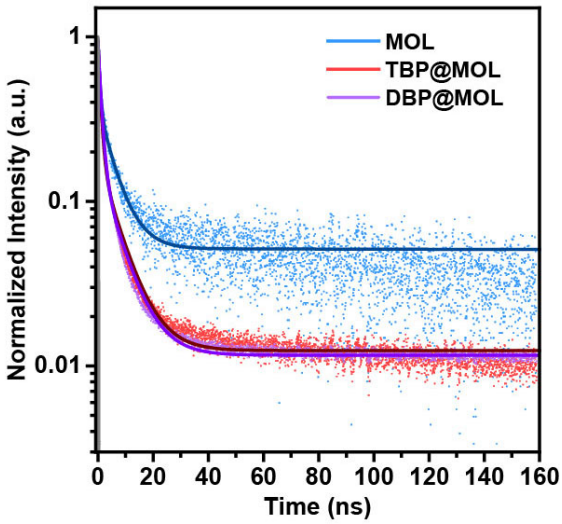

Figure S37. Fluorescence decays of the DBB-Ir chromophores in TBP@MOL, DBP@MOL, and MOL using time-correlated single photon counting (TCSPC). Measurements were obtained using water dispersions of TBP@MOL, DBP@MOL, and MOL at equivalent DBB-Ir concentrations of 0.2 μM (λ_{ex} = 403 nm, λ_{em} = 550 ± 40 nm). Solid lines represent the fits of the correspondingly colored data points.

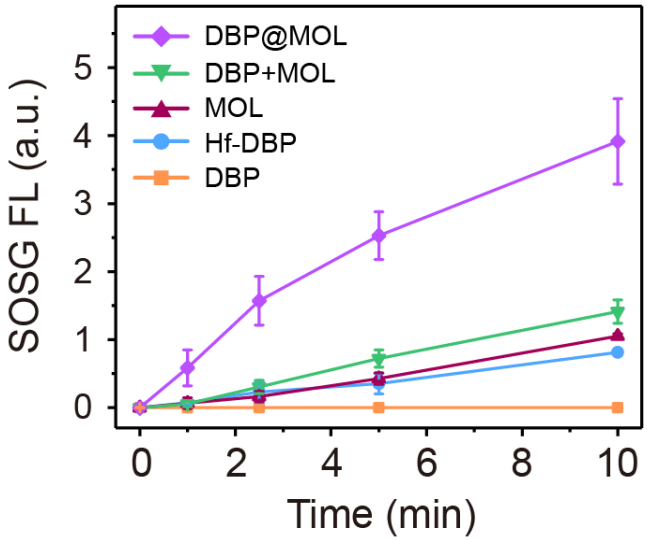

Figure S38. $^1O_2$ generation of various sonosensitizers with US irradiation. SOSG fluorescence curves of the DBP systems after US irradiation in water, showing that DBP@MOL has the highest $^1O_2$ generation.

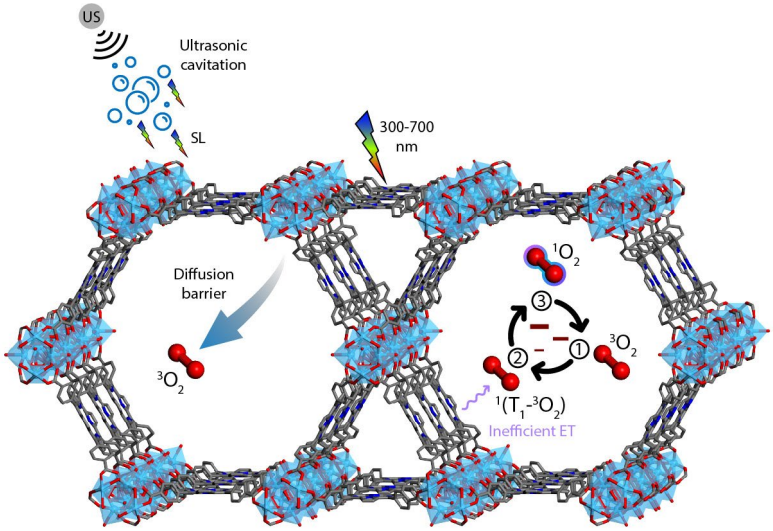

Figure S39. Proposed mechanism of $^1O_2$ generation for Hf-TBP under ultrasound. Mechanism of $^1O_2$ generation for Hf-TBP under US irradiation and excitation from broad-spectrum SL (rainbow bolt) illustrating its lower sensitizing ability (red minus), which is due to the lack of a donor ligand and less efficient energy transfer (ET; purple arrows) from rigidly confined TBP in the sensitizer-oxygen encounter complex, $^1(T_1\text{-}^3O_2)$.

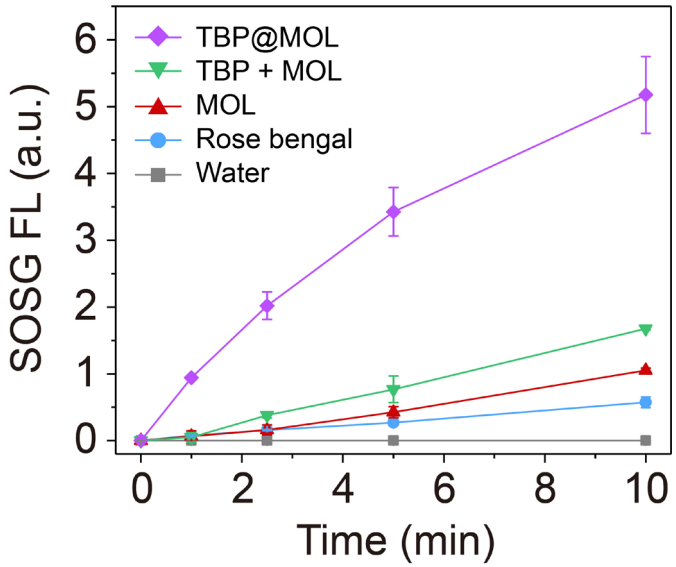

Figure S40. Singlet oxygen generation of TBP@MOL, TBP + MOL, MOL, rose bengal and water upon ultrasound irradiation, detected by SOSG assay.

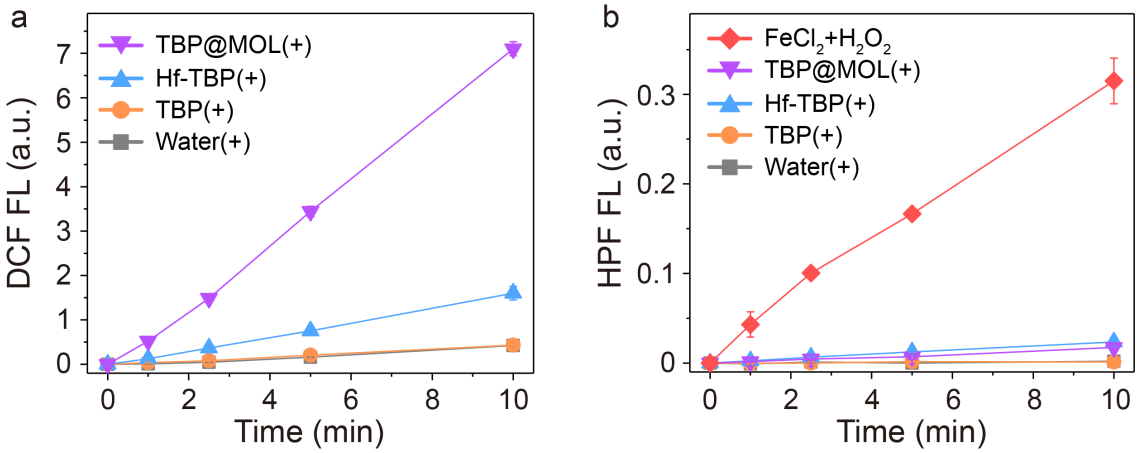

Figure S41. (a) ROS generation of different TBP systems upon ultrasound irradiation as detected by DCF assay. (b) Hydroxyl radical generation of different TBP systems upon ultrasound irradiation and a mixture of $FeCl_2$ and H_2O_2 (as a positive control for hydroxyl radical generation), as detected by HPF assay.

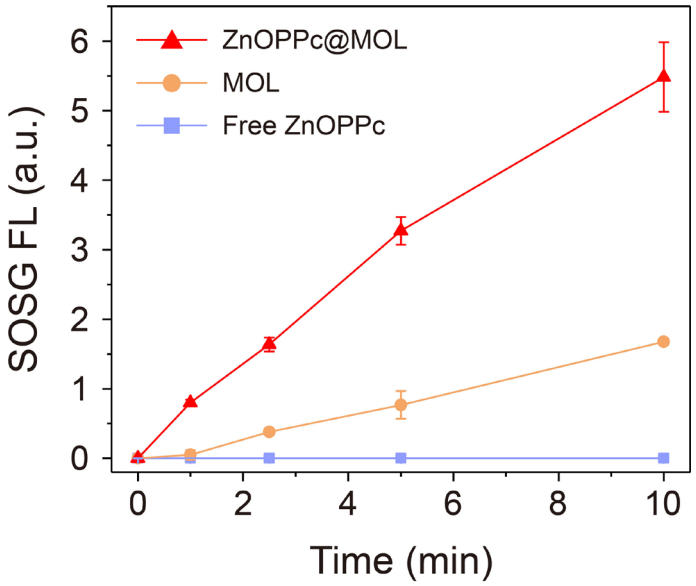

Figure S42. Singlet oxygen generation of ZnOPPc@MOL, MOL, and free ZnOPPc [zinc(II)-2,3,9,10,16,17,23,24-octa(4-carboxyphenyl)phthalocyanine] upon ultrasound irradiation as detected by SOSG assay.

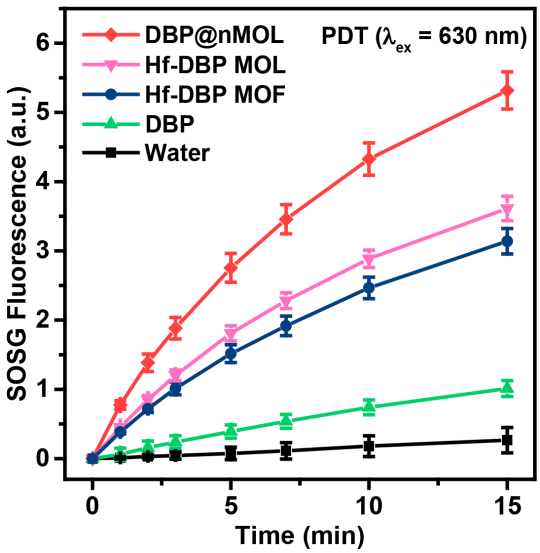

Figure S43. $^1O_2$ generation of DBP sensitizers with visible light irradiation. SOSG fluorescence curves for the DBP systems after visible light irradiation in water. Unlike US irradiation, visible light irradiation at 630 nm only excites the DBP chromophore in the DBP@MOL system, so there is no possibility of donor-acceptor energy transfer from DBB-Ir to DBP. DBP@MOL exhibits the highest efficacy over both systems. Since DBP@MOL does not differ significantly from Hf-DBP MOF in steady-state or time-resolved fluorescence spectroscopy, we postulate that the loosely surface-anchored DBP is more efficient at sensitizing $^3O_2$ than the rigid framework-confined DBP.

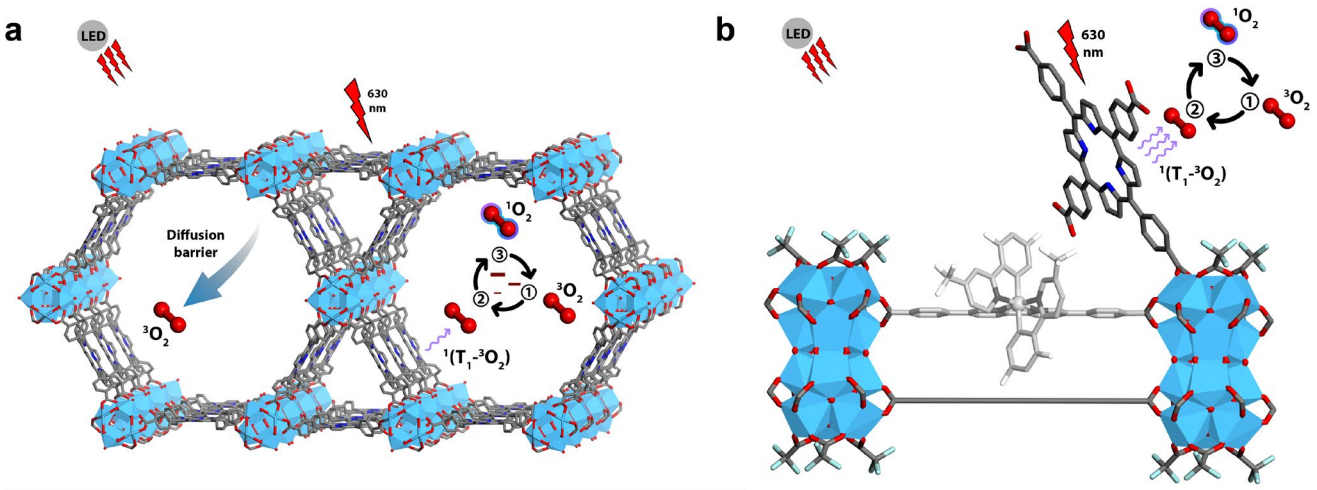

Figure S44. Mechanism of $^1O_2$ generation for Hf-TBP and TBP@MOL. (a) Proposed mechanistic model of the less efficient $^1O_2$ generation by Hf-TBP. The TBP chromophores are rigidly bound within the framework of the 3D MOF, which means that $^3O_2$ must diffuse through the framework to access excited TBP sensitizers and then $^1O_2$ must diffuse back out. Additionally, since the energy transfer between the excited sensitizer-oxygen encounter complex, $^1(T_1\text{-}^3O_2)$, proceeds via internal conversion (IC),[9] we postulate that oxygen sensitization is primarily less efficient due to the rigidity of the TBP sensitizers. (b) Proposed mechanistic model of the efficient $^1O_2$ generation by TBP@MOL. The light irradiation at 630 nm only excites the TBP chromophores, so the DBB-Ir chromophore is inactive under PDT conditions (greyed out). We postulate that the 2D MOL morphology and surface-anchored TBP allows $^3O_2$ to have barrierless access to both faces of the sensitizer which, in combination with the relative flexibility of the TBP, facilitates better encounter complex energy transfer and sensitization efficiency.

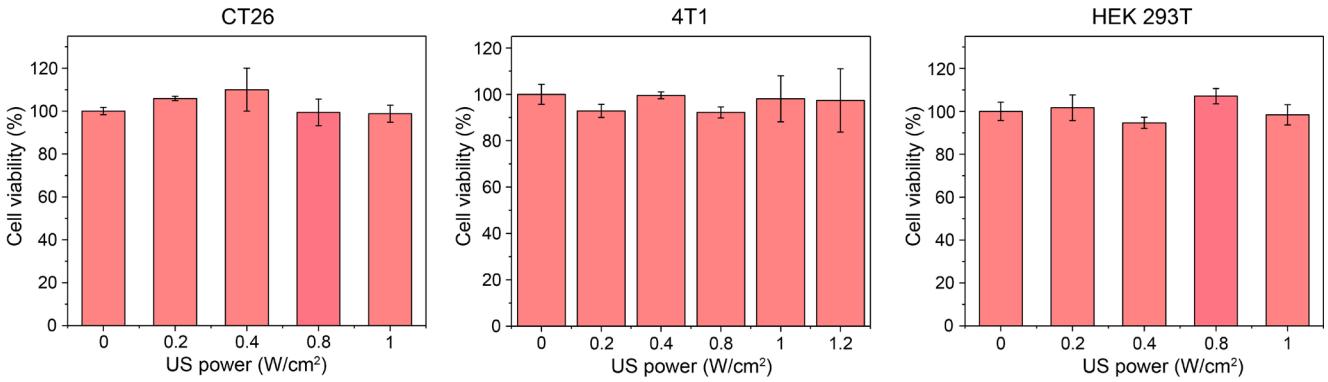

Figure S45. Viability of CT26, 4T1, and HEK 293T cells upon ultrasound irradiation at different power densities.

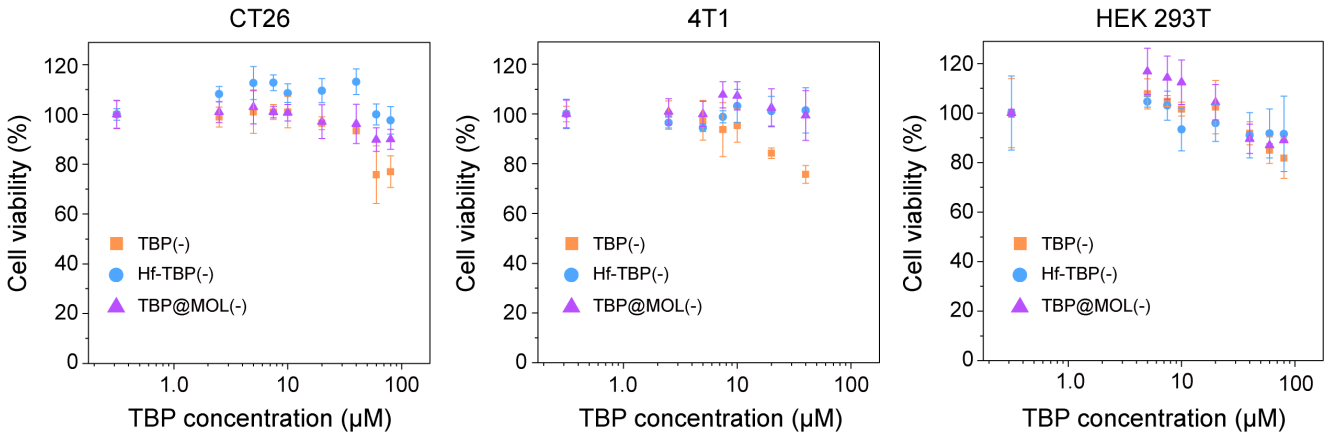

Figure S46. Viability of CT26, 4T1, and HEK 293T cells treated with TBP(-), Hf-TBP(-), or TBP@MOL(-).

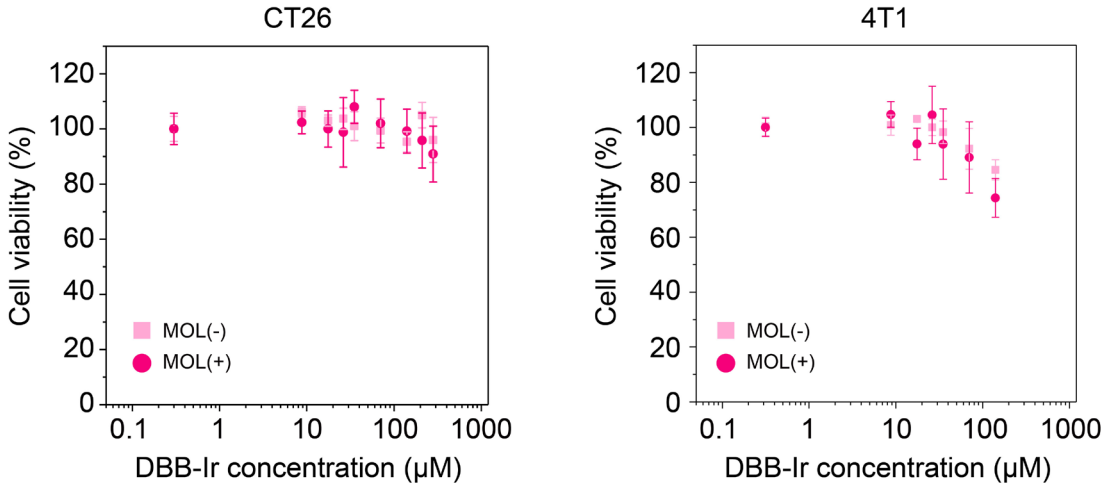

Figure S47. Viability of CT26 and 4T1 cells treated with MOL(-) and MOL(+).

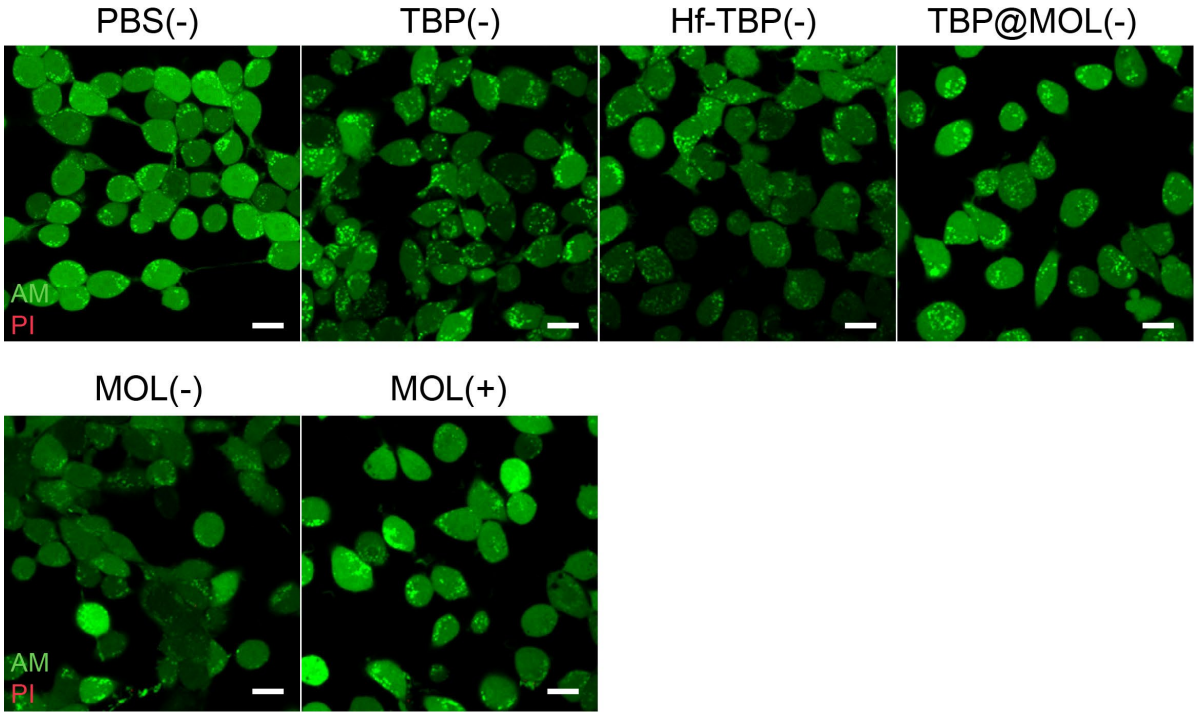

Figure S48. AM/PI (live/death) staining of CT26 cells after PBS(-), TBP(-), Hf-TBP(-), TBP@MOL(-), MOL(-), or MOL(+) treatment. (Scale bar: 20 μm)

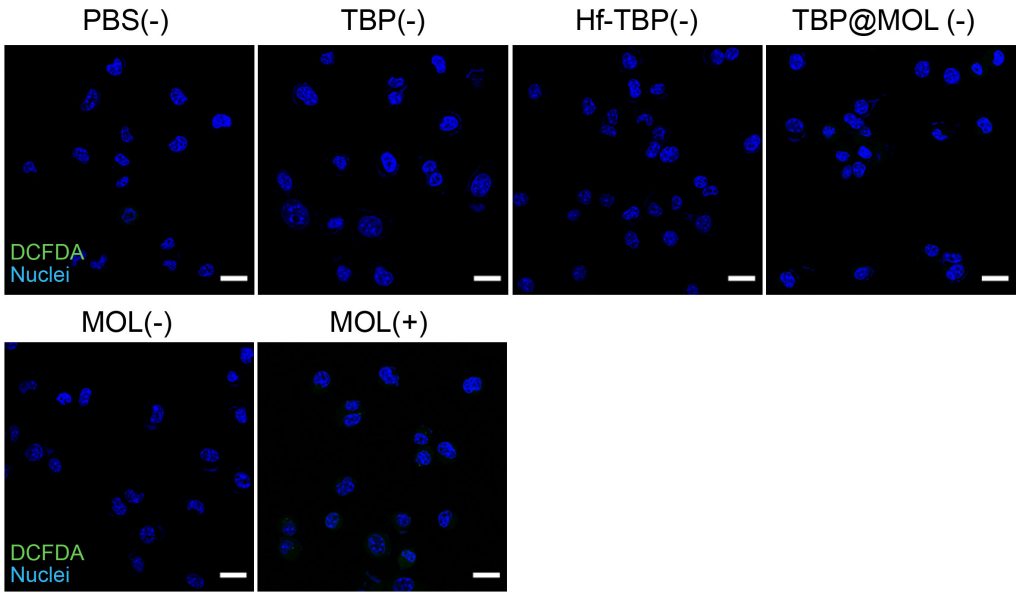

Figure S49. CLSM of ROS generation in CT26 cells after PBS(-), TBP(-), Hf-TBP(-), TBP@MOL(-), MOL(-), or MOL(+) treatment. (DCF-DA, green; Hoechst, blue; scale bar = 20 μm)

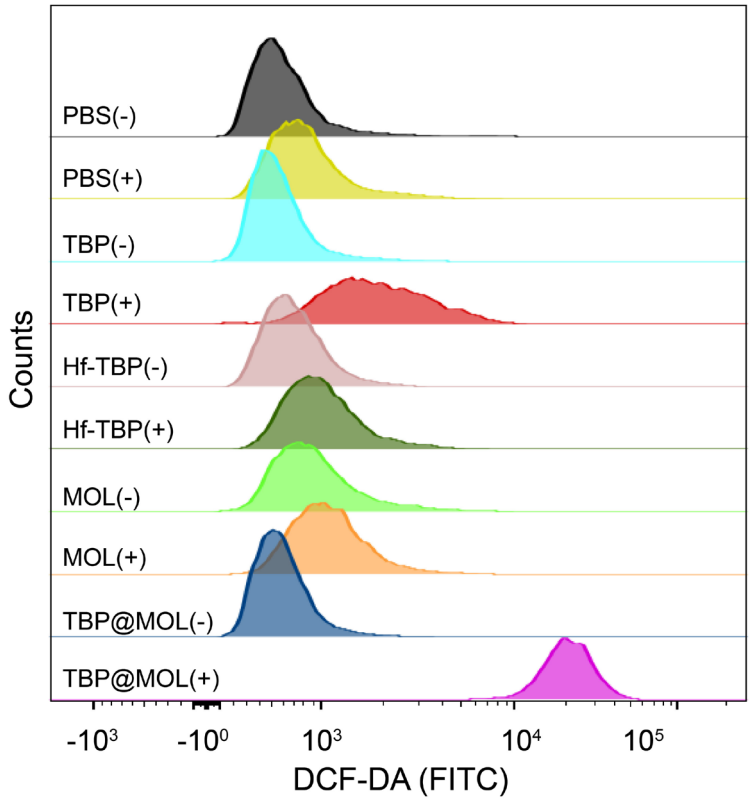

Group	MFI
PBS(-)	570
PBS(+)	786
TBP(-)	537
TBP(+)	1801
Hf-TBP(-)	685
Hf-TBP(+)	968
MOL(-)	860
MOL(+)	1063
TBP@MOL(-)	574
TBP@MOL(+)	20862

Figure S50. Quantification of intracellular ROS signals in CT26 cells after different treatments by flow cytometry.

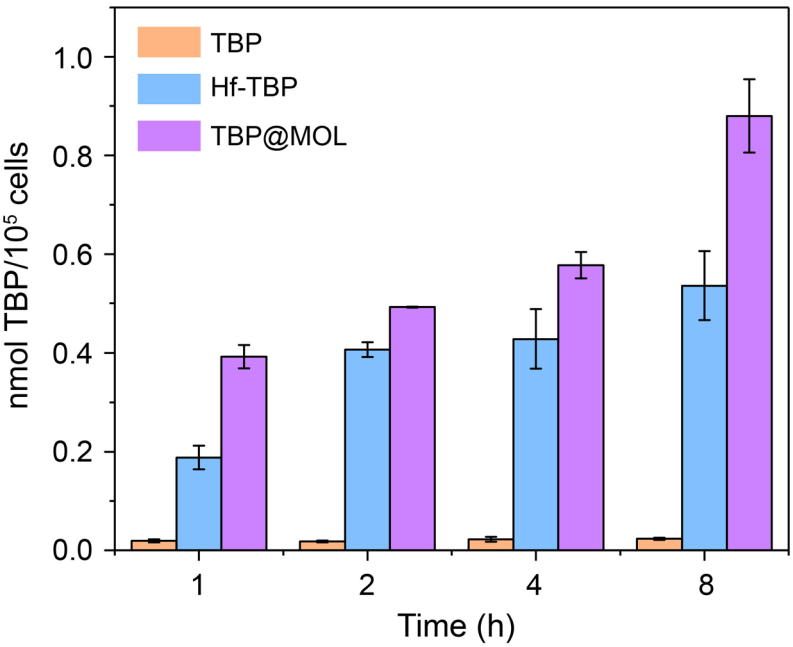

Figure S51. Intracellular uptake of TBP, Hf-TBP, or TBP@MOL at different time points determined by UV-Vis spectroscopy.

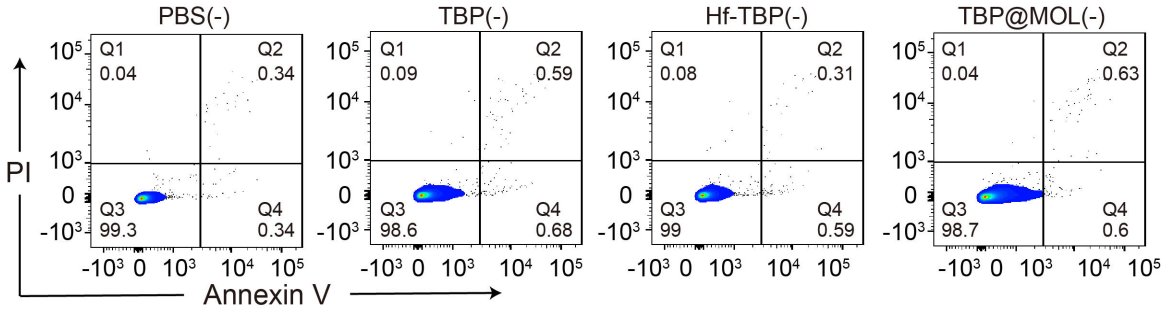

Figure S52. Flow cytometric analyses of Annexin V/PI staining of CT26 cells after PBS(-), TBP(-), Hf-TBP(-), or TBP@MOL(-) treatment.

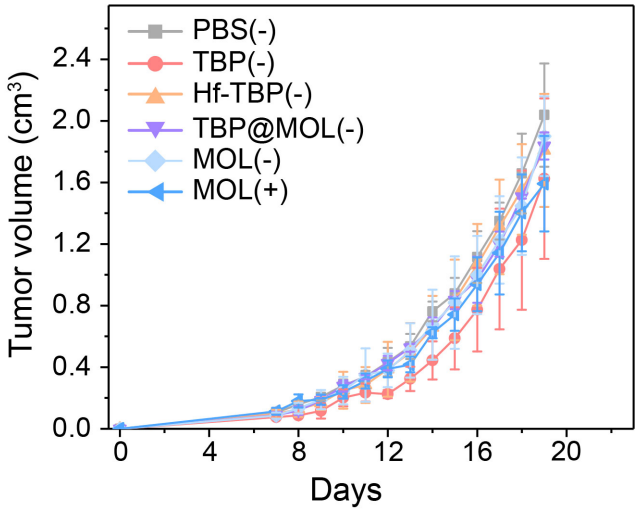

Figure S53. Tumor volume curves of CT26 tumor-bearing BALB/c mice in control groups.

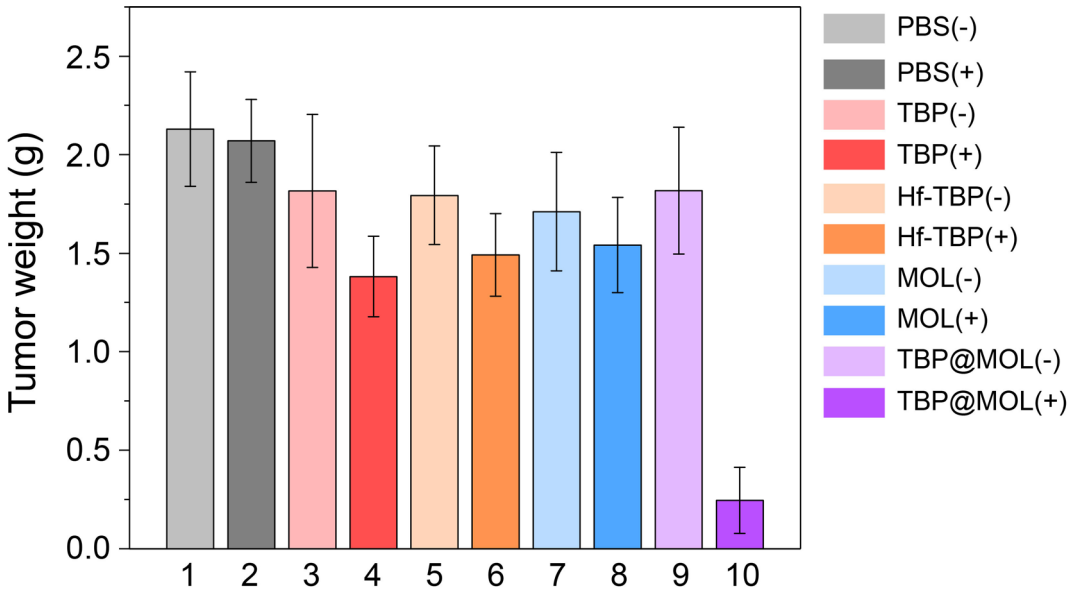

Figure S54. Weights of excised CT26 tumors of BALB/c mice in all groups.

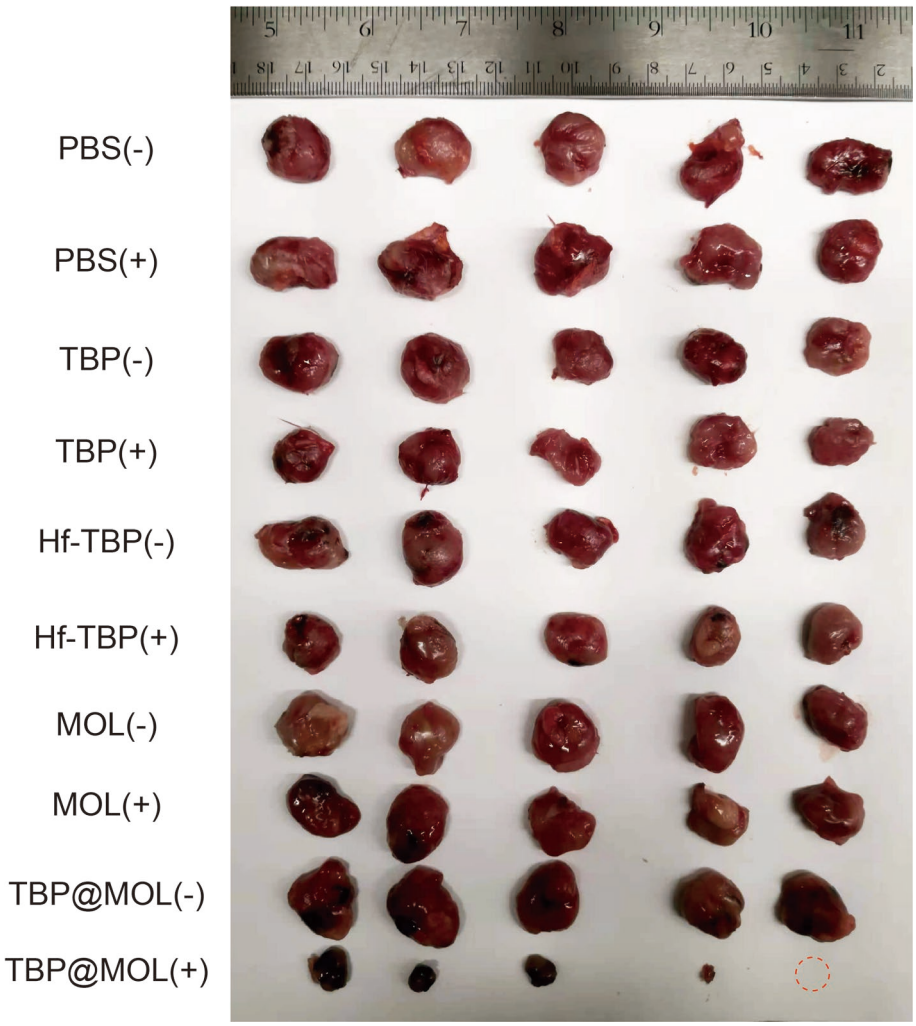

Figure S55. Photograph of excised CT26 tumors of BALB/c mice in all groups.

.

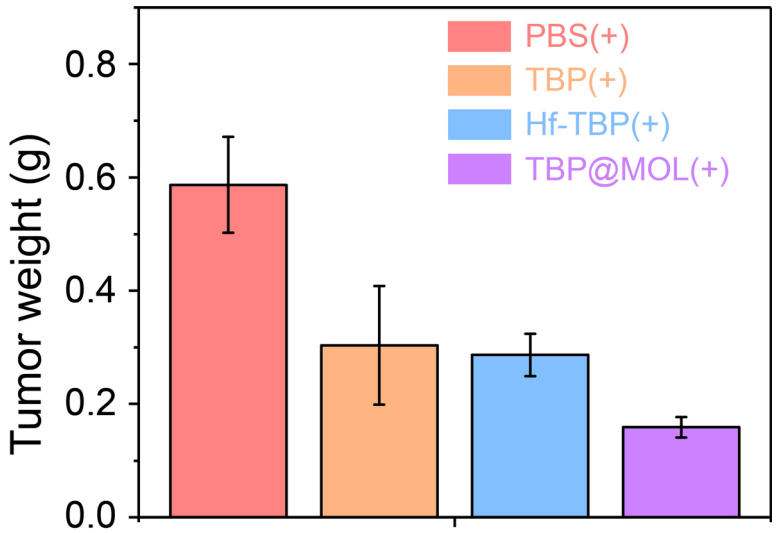

Figure S56. Weight of excised 4T1 tumors of BALB/c mice after the treatment of PBS(+), TBP(+), Hf-TBP(+), or TBP@MOL(+) treatment.

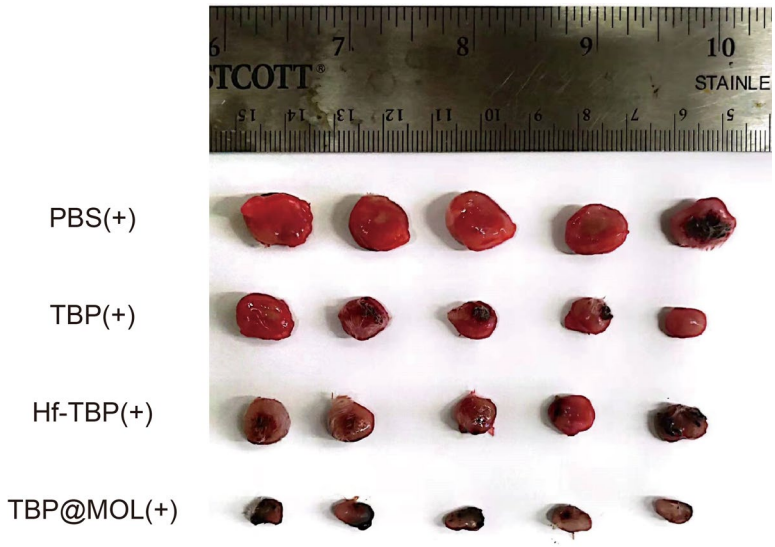

Figure S57. Photograph of excised 4T1 tumors of BALB/c mice after the treatment of PBS(+), TBP(+), Hf-TBP(+), or TBP@MOL(+) treatment.

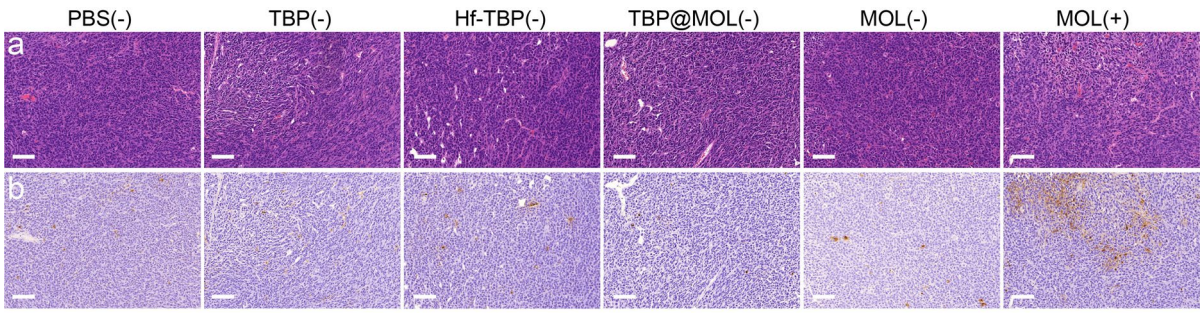

Figure S58. H&E (a) and TUNEL (b) staining of excised CT26 tumor sections in different control groups. (Scale bar: 100 μm)

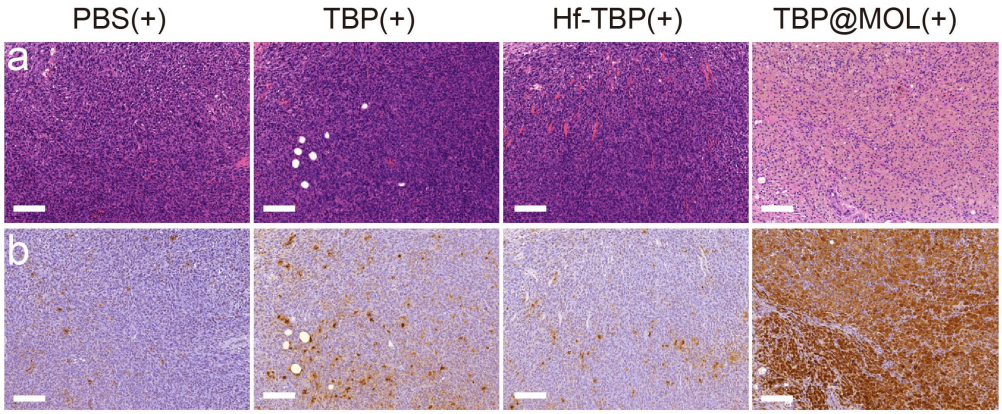

Figure S59. H&E (a) and TUNEL (b) staining of excised 4T1 tumor sections after PBS(+), TBP(+), Hf-TBP(+), or TBP@MOL(+) treatment. (Scale bar: 100 μm)

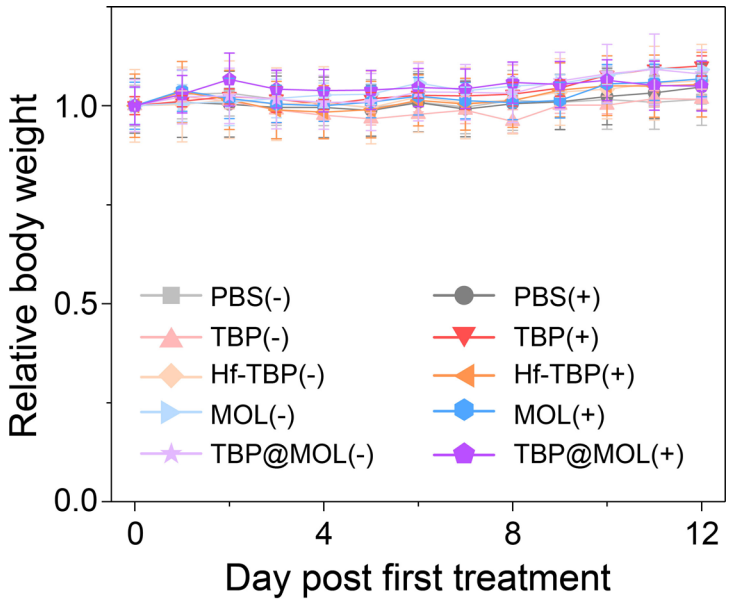

Figure S60. Relative body weight curves of CT26 tumor-bearing BALB/c mice in all treatment groups.

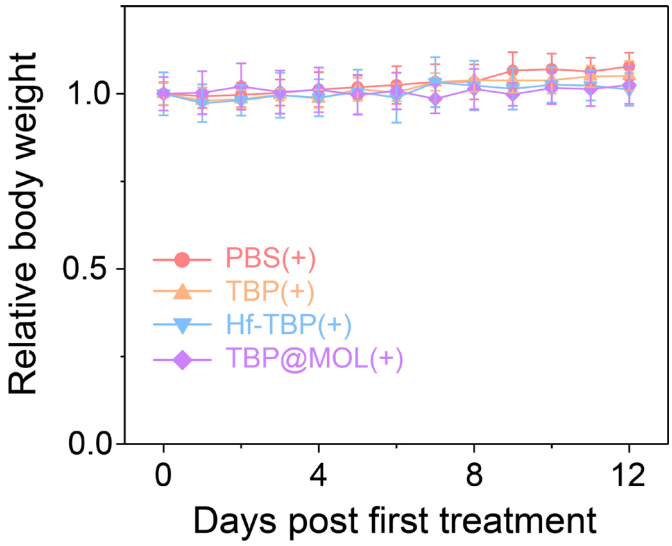

Figure S61. Relative body weight curves of 4T1 tumor-bearing BALB/c mice in treatment groups.

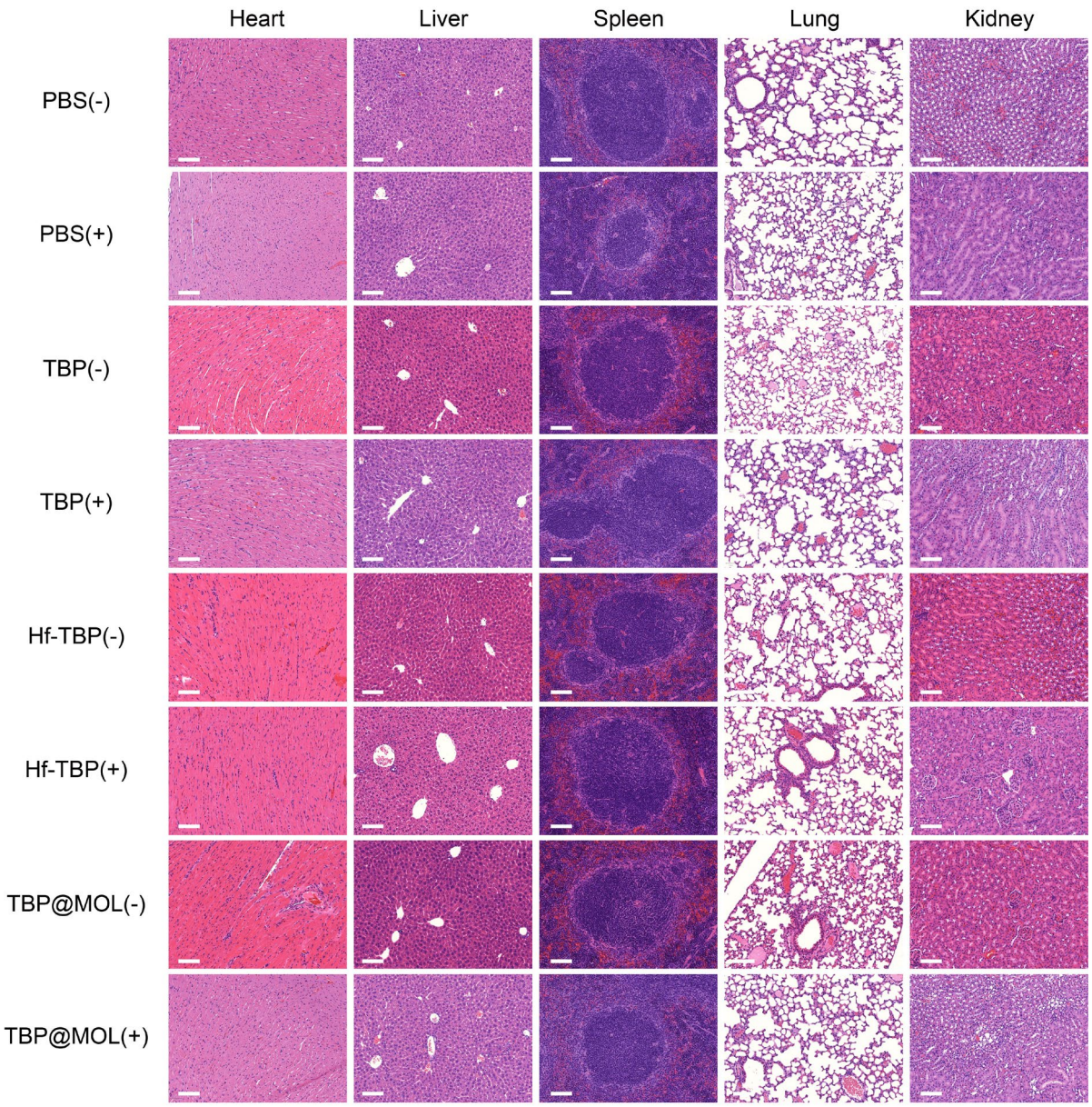

Figure S62. H&E staining of major organs from CT26 tumor-bearing mice in treated and control groups. (Scale bar = 100 μm)

References

[1] P. Bankhead, M. B. Loughrey, J. A. Fernández, Y. Dombrowski, D. G. McArt, P. D. Dunne, S. McQuaid, R. T. Gray, L. J. Murray, H. G. Coleman, J. A. James, M. Salto-Tellez, P. W. Hamilton, Scientific Reports **2017**, 7, 16878.

[2] Y.-Y. Zhu, G. Lan, Y. Fan, S. S. Veroneau, Y. Song, D. Micheroni, W. Lin, Angewandte Chemie International Edition **2018**, 57, 14090.

[3] G. T. Nash, T. Luo, G. Lan, K. Ni, M. Kaufmann, W. Lin, Journal of the American Chemical Society **2021**, 143, 2194.

[4] K. Lu, C. He, N. Guo, C. Chan, K. Ni, R. R. Weichselbaum, W. Lin, Journal of the American Chemical Society **2016**, 138, 12502.

[5] K. Lu, C. He, W. Lin, Journal of the American Chemical Society **2014**, 136, 16712.

[6] K. Lu, C. He, N. Guo, C. Chan, K. Ni, G. Lan, H. Tang, C. Pelizzari, Y.-X. Fu, M. T. Spiotto, R. R. Weichselbaum, W. Lin, Nature Biomedical Engineering **2018**, 2, 600.

[7] T. Luo, Y. Fan, J. Mao, E. Yuan, E. You, Z. Xu, W. Lin, Journal of the American Chemical Society **2022**, 144, 5241.

[8] T. Prozorov, R. Prozorov, K. S. Suslick, Journal of the American Chemical Society **2004**, 126, 13890.

[9] R. Schmidt, Photochemistry and Photobiology **2006**, 82, 1161.